MEMS-Tunable Vertical-Cavity SOAs

Garrett D. Cole, E. Staffan Björlin, *Member, IEEE*, Qi Chen, Chung-Yeung Chan, *Student Member, IEEE*,
Shaomin Wu, Chad S. Wang, *Student Member, IEEE*, Noel C. MacDonald, *Fellow, IEEE*, and
John E. Bowers, *Fellow, IEEE*

Abstract—We present the signal gain, wavelength tuning characteristics, saturation properties, and noise figure (NF) of MEMS-based widely tunable vertical-cavity semiconductor optical amplifiers (VCSOAs) for various optical cavity designs, and we compare the theoretical results to data generated from a number of experimental devices. Using general Fabry–Pérot relationships, it is possible to model both the wavelength tuning characteristics and the peak signal gain of tunable vertical-cavity amplifiers, while a rate-equation analysis is used to describe the saturation output power and NF as a function of the VCSOA resonant wavelength. Additionally, the basic design principles for an integrated electrostatic actuator are outlined. It is found that MEMS-tunable VCSOAs follow many of the same design trends as fixed-wavelength devices. However, with tunable devices, the effects of varying mirror reflectance and varying single-pass gain associated with the MEMS-based tuning mechanism lead to changing amplifier properties over the wavelength span of the device.

Index Terms—Fabry–Pérot resonators, laser amplifiers, microelectromechanical devices, optical pumping, semiconductor optical amplifiers, surface-emitting lasers, tunable amplifiers, wafer bonding.

I. INTRODUCTION

LONG-WAVELENGTH vertical-cavity semiconductor optical amplifiers (VCSOAs) are attractive as a low-cost alternative to erbium-doped fiber amplifiers (EDFAs) and conventional in-plane SOAs for use in fiber-optic communication systems such as metro-area networks and fiber to the home. In such applications, VCSOAs benefit from a high coupling efficiency to optical fiber, polarization-independent gain, the potential to fabricate two-dimensional (2-D) arrays, and the ability to test devices on wafer. Additionally, by altering the composition of the active material, amplification may be achieved at any desired wavelength, in contrast with the limited wavelength

range of fiber amplifiers. In recent years, both optically and electrically pumped long-wavelength VCSOAs have been demonstrated [1]–[4].

The high-finesse Fabry–Pérot (FP) cavity of VCSOAs results in a narrow gain bandwidth. This inherent filtering effect is advantageous, as it eliminates out-of-band noise and provides channel selection in multiwavelength systems. Additionally, the narrow gain spectrum eliminates the need for an optical filter after the amplifier, thereby further reducing cost [5]. However, in low-cost systems, uncooled sources are typically used, and the signal wavelength can vary over a fairly wide range. If the signal wavelength deviates only slightly from the peak gain wavelength of the VCSOA, distortion of the signal may result. It is therefore of great interest to make tunable VCSOAs that can cover a wider wavelength range and can be precisely adjusted to match the wavelength of the signal. Previously, temperature tuning of long-wavelength VCSOAs has been investigated [6], but a more promising approach is microelectromechanical (MEMS) tuning. In this case, mechanical alteration of the effective FP mode gives rise to tuning ranges greater than those that can be achieved by refractive index modulation. Recently, both electrically and optically pumped vertical-cavity surface-emitting lasers (VCSELs) with >30-nm single-mode tuning ranges have been demonstrated [7], [8]. We report here the first widely tunable semiconductor optical amplifier, using a MEMS-based tuning element to sweep the narrow gain bandwidth of the VCSOA over the wavelength span of the device, resulting in tunable channel-selective amplification [9].

As with the VCSEL and the in-plane laser diode, the vertical-cavity geometry of VCSOAs gives rise to major differences in amplifier properties when compared to in-plane FP-SOAs. The relatively short cavity length, which lies perpendicular to the plane of the wafer surface, results in a small mode volume and a circular symmetric mode. In addition, the optical field passes perpendicularly through the material layers, greatly reducing the active material length with which the optical mode overlaps, resulting in a large reduction in the achievable single-pass gain. For the case of in-plane SOAs, the active material length may be on the order of hundreds of micrometers, whereas in a VCSOA the combined thickness of the multiquantum-well (MQW) layers may be on the order of 100 nm. The reduction in single-pass gain requires a corresponding increase in feedback necessary to achieve a desired gain level. As with VCSELs, this feedback is achieved by incorporating highly reflective distributed Bragg reflectors (DBRs) to create an FP optical cavity. The resulting feedback from the resonant cavity structure constricts the gain bandwidth to the linewidth of the FP mode, which is typically on the order of a nanometer or less.
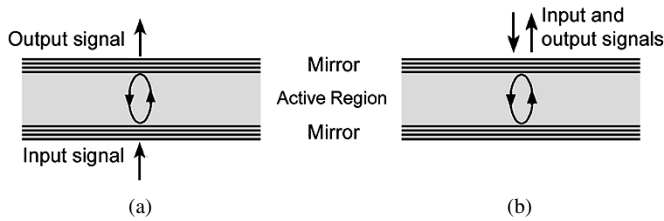
Fig. 1. Schematic of the operating modes of VCSOAs, including (a) transmission mode and (b) reflection mode.

The most significant difference when comparing VCSOAs and VCSELs lies in the reduced mirror reflectivities used in the resonant cavity structure, as well as the increased number of QWs necessary to achieve a high single-pass gain. With VCSELs, strong feedback is desired to reduce the threshold current; however, the opposite is true for VCSOAs. For the VCSOA, the feedback supplied by the DBR mirrors must be reduced. If the feedback is high enough to compensate for the cavity losses, the device will start lasing, resulting in gain clamping at threshold. Low mirror reflectance allows for operation at an increased carrier density and thus higher single-pass gain. In general, the use of reduced mirror reflectance leads to a wider gain bandwidth, higher saturation power, and a reduced noise figure (NF) [10]–[12]. It is important to recognize that there is a limit to the lowest mirror reflectance that may be used; if the reflectance is too low, the mirror losses will result in insufficient signal gain. With VCOSAs, there exists an optimum design with an intermediate reflectance that allows for operation at increased carrier density while at the same time avoiding exceeding the lasing threshold. Another important difference between VCSELs and VCSOAs is the number of active material layers used in the device. The need for increased single-pass gain requires the incorporation of a large number of QWs in the FP resonant cavity. With VCSOAs, a stacked MQW active region is used to increase the total active material length in the inherently short optical cavity.

There are two operating modes possible with VCSOAs: reflection-mode and transmission-mode operation. In reflection mode, the VCSOA is designed to have one highly reflective mirror ($\sim$100%), and the signal enters and exits from the same side of the device through a slightly transmissive mirror, as seen in Fig. 1. In transmission-mode operation, both mirrors are slightly transmissive and the signal is injected on one side of the device and collected on the other. The choice of the mode of operation, either reflection-mode or transmission-mode, will ultimately depend on the intended application.

Although little previous work has focused specifically on MEMS-tunable VCSOAs (MT-VCSOAs), a number of research groups have developed a variety of other MEMS-tunable vertical-cavity devices, including VCSELs [7], [8], [13]–[15], resonant-cavity light-emitting diodes (RCLEDs) [16], asymmetric FP modulators [17], and vertical-cavity filters [18]. The majority of these structures have utilized electrostatic tuning, although thermal tuning is also frequently used [7]. Recently, we demonstrated the first MT-VCSOA [9]. The devices were constructed using a combination of InP-GaAs wafer bonding and AlGaAs-based micromachining and utilized an integrated electrostatic tuning element for wavelength selection. The

MT-VCSOA is operated in reflection mode and is optically pumped with a 980-nm diode laser, similar to previous generations of nontunable vertical-cavity amplifiers. The best performance parameters measured with the first generation of tunable VCSOAs was 10 dB of device gain (3 dB fiber-to-fiber) over a tuning range of 11 nm, as well as a peak signal gain of 17 dB (10 dB fiber-to-fiber) [9]. We present here a second generation of devices utilizing a revised mechanical structure that greatly reduces the required tuning voltages and increases the wavelength tuning range of the MT-VCSOA. To further improve the performance of these devices, a more detailed understanding of the possible design options is developed.

In this paper, we will review the design and characteristics of MT-VCSOAs. Using a general FP model, we are able to analyze both the tuning and signal gain properties of MT-VC-SOAs. With the amplifier rate equations, the saturation and noise characteristics of these unique devices may be illustrated. In Section II, an overview of the theoretical models and the various cavity designs available for MEMS-tunable vertical-cavity amplifiers is presented. Following this, the basic properties of electrostatic actuation and the mechanical properties of the MEMS tuning element are covered in Section III. The device structure and fabrication process is discussed in Section IV. In Section V, we present the experimental testing procedure as well as recent results, and, using the models developed in Section II, the wavelength tuning response, peak signal gain, saturation output power, and amplifier noise figure is determined for various cavity designs and modes of operation.

II. THEORETICAL MODEL

A. Signal Gain

A convenient approach for modeling VCSOAs is to replace the DBRs by hard mirrors of the same reflectance and use an effective cavity length, which includes the penetration of the optical field into the DBRs [19]. With this method, we can use the well-known FP relationships to describe both the amplifier and wavelength tuning characteristics of the MT-VCSOA. Because the FP equations contain only a small number of unknowns, it is possible to generate a relatively general description of the device properties. The FP approach is carried out by considering an incoming optical field and summing all of the field components exiting the cavity. To obtain the power gain, the fields are squared and the total output power is divided by the input power. Using this technique, it is possible to model the gain spectrum of a VCSOA for both reflection-mode (G_r) and transmission-mode (G_t) operation [20]

$$G_r = \frac{(\sqrt{R_t} - \sqrt{R_b}g_s)^2 + 4\sqrt{R_tR_b}g_s\sin^2\phi_s}{(1 - \sqrt{R_tR_b}g_s)^2 + 4\sqrt{R_tR_b}g_s\sin^2\phi_s} \quad (1)$$

$$G_t = \frac{(1 - R_t)(1 - R_b)g_s}{(1 - \sqrt{R_tR_b}g_s)^2 + 4\sqrt{R_tR_b}g_s\sin^2\phi_s} \quad (2)$$

$$\phi_s = 2\pi n_c L_c \left(\frac{1}{\lambda} - \frac{1}{\lambda_R}\right) \quad (3)$$

where R_t is the top mirror reflectance, R_b is the bottom mirror reflectance, g_s is the single-pass gain, and ϕ_s is the single-pass phase detuning. The phase in (3) gives the deviation of the signal wavelength λ from the resonant wavelength of the cavity λ_R,

with the effective index of the optical cavity n_c and the total cavity length L_c. When the signal wavelength is identical to the FP resonance, $\phi_s = 0$ in (3) and (1) and (2) can be used to calculate the peak gain. It is important to note that, in each case, the amplifier must operate under the condition of $G_s^2 R_t R_b < 1$ to avoid exceeding the lasing threshold. Assuming uniform active material over the extent of the signal spot size, the single-pass gain of the VCSOA is calculated using

$$g_s = \exp[\xi g L_a - \alpha_i L_c] \tag{4}$$

with the combined thickness of the QWs L_a, the average cavity loss α_i, the total cavity length L_c—including the penetration depth into the mirrors—and the gain-enhancement factor ξ. With vertical-cavity devices, standing wave effects must be considered. In this case, gain enhancement results from the placement of the active material layers at the peaks of the optical standing wave, and ξ is given by [21]

$$\xi = 1 + \cos 2\beta z_s \frac{\sin \beta L_{\mathrm{MQW}}}{\beta L_{\mathrm{MQW}}} \tag{5}$$

where L_{MQW} is the thickness of each MQW stack, $\beta = 2\pi n_c/\lambda$, n_c is the effective index of the semiconductor cavity, and z_s is the spatial separation between the standing wave peak and the center of the MQW stack. This form of ξ is useful for determining the change in gain enhancement that occurs with wavelength tuning. The gain enhancement factor can be 2 for very small values of L_{MQW} and quickly converges to a value of 1 for QWs distributed over a section longer than a wavelength. In practice, ξ is usually less than 2 due to the finite thickness of the gain region. The QW material gain g as a function of carrier density N is approximated using a three-parameter model [22]

$$g = g_o \ln \left[\frac{N + N_s}{N_{\mathrm{tr}} + N_s} \right] \tag{6}$$

with the transparency carrier density N_{tr} and fitting parameters g_o and N_s. This model allows for an accurate description of the material gain at low carrier densities, however, for very high carrier densities, the logarithmic gain model may be limited, as it does not predict saturation of the material gain.

B. Saturation and Noise Figure

At high input signal powers, or at operation near threshold, the large photon density present in the resonant cavity will lead to carrier depletion and saturation of the gain medium. A common approach to modeling the saturation properties of VCSOAs involves the use of steady-state rate equations for carriers and photons [10]–[12]. Compared to the well-known relationships used to analyze lasers, the rate equations for FP amplifiers include an additional term for the input signal and a modified mirror loss term. The rate equations for carriers N and photons S then take the following form:

$$\frac{dN}{dt} = G_{\mathrm{gen}} - \xi v_g g S - (AN + BN^2 + CN^3) \tag{7}$$

$$\frac{dS}{dt} = \frac{\eta_s P_s}{h v_s A_s L_c} + \beta_{\mathrm{sp}} \Gamma B N^2 + \xi \Gamma v_g g S - (\alpha_i + \alpha_m) v_g S. \tag{8}$$

The first term on the right-hand side of (7), G_{gen}, is a carrier generation term that depends on whether optical or electrical pumping is used. For optically pumped devices, such as those presented here, $G_{\mathrm{gen}} = \eta_p P_p/h v_p V_p$ with the pump efficiency η_p, the pump power P_p, the energy of the pump photons $h v_p$, and the pumped volume $V_p = L_a A_p$ (A_p is the area of the pump spot). The second term describes stimulated emission and includes the group velocity v_g. The final term constitutes all recombination parameters that do not contribute to amplification of the input signal: AN describes defect recombination, BN^2 is spontaneous emission, and CN^3 is Auger recombination. The second rate equation summarizes the physical mechanisms that affect the average photon density S. The first term on the right-hand side of (8) describes the increase in photon density resulting from the injected signal of power P_s and energy $h v_s$. The signal coupling efficiency η_s and the signal spot size A_s complete the first term. The next two terms represent the generation of photons through spontaneous and stimulated emission, respectively. The coefficient β_{sp} describes the fraction of spontaneously emitted photons coupled into the signal mode, with the fill factor $\Gamma = L_a/L_c$. The final term in (8) describes photon loss, due to both cavity and mirror losses. For VCSOAs, α_m is described by a modified mirror loss expression which is a function of the mirror reflectance and the amplifier gain [23]

$$\alpha_m = \frac{1}{L_c} \left(\frac{G_r + G_t}{G_r + G_t - 1} \right) \ln g_s. \tag{9}$$

Using the procedure outlined in [11], the steady-state forms of (7) and (8) may be used to determine the saturation characteristics of the MT-VCSOA.

The NF of an optical amplifier describes the signal-to-noise ratio (SNR) degradation that occurs as a signal passes through the device. In general, the amplification of an optical signal adds undesired power fluctuations due to the inherent randomness of the optical processes involved. With a vertical-cavity amplifier, the dominant noise component at high signal powers is signal-spontaneous beat noise [10], [12]. The NF F, defined as the input SNR over output SNR, is given by

$$F = 2 n_{\mathrm{sp}} \chi \left(\frac{G - 1}{G} \right) \tag{10}$$

where n_{sp} is the population inversion parameter ($n_{\mathrm{sp}} = N/N - N_{\mathrm{tr}}$), G is the signal gain, and χ is the excess noise coefficient, which describes signal-spontaneous beat noise enhancement due to finite mirror reflectivity (the NF is defined as $\mathrm{NF} = 10 \log(F)$ and is expressed in decibels). For reflection- and transmission-mode operation, χ becomes [24]

$$\chi_r = \frac{(1 + R_b g_s)(g_s - 1)}{(R_b g_s^2 - 1)} \tag{11}$$

$$\chi_t = \frac{(1 + R_b g_s)(1 - R_t)(g_s - 1)}{(1 - R_b)(1 - R_t) - (1 - \sqrt{R_b R_t} g_s)^2}. \tag{12}$$

For a reflection-mode device, χ_r depends only on the bottom mirror reflectivity, and, for values of R_b greater than 0.999, $\chi_r \approx 1$. In the case of transmission-mode VCSOAs, the excess noise coefficient equals one for single-pass gain values of $g_s = R_b^{-1/2}$. The population inversion parameter n_{sp} equals one for complete inversion and increases for incomplete inversion. From (10), it is desirable to operate at high carrier densities
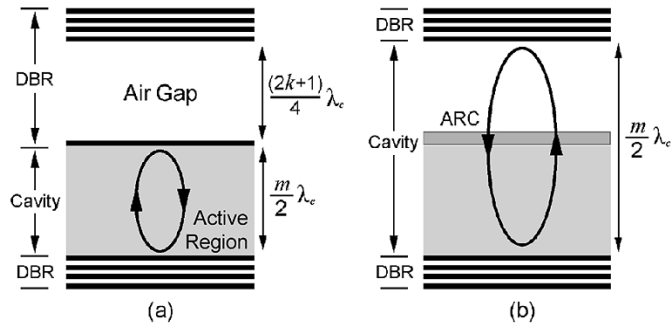
Fig. 2. Schematic of the (a) SCC and (b) EC designs. For each configuration, the mirror reference planes have been defined so that the DBR begins with a high index layer (black line). Additionally, the mirrors are designed to give a π phase shift at λ_c, and m and k are integers. In (a), the semiconductor active region is of a resonant thickness and the air gap serves as a low index layer of the top DBR. With the extended cavity structure shown in (b), the incorporation of an antireflection coating (ARC) creates a distributed cavity of a total length $m\lambda_c/2$. The circulating arrows indicate the position of maximum intensity of the optical standing wave.

in order to minimize n_{sp}. Unfortunately, high carrier densities may lead to lasing; it is therefore important to reduce the mirror reflectance in order to allow for full inversion without reaching the point of self-sustaining oscillation, while still maintaining sufficient reflectance to achieve the desired level of signal gain. Note that the important parameter when regarding noise in any amplifier application is the fiber-to-fiber noise figure. In this instance, the superior coupling efficiency of VCSOAs, as compared to in-plane SOAs, becomes a clear advantage.

C. Tunable Cavity Design

In addition to standing wave effects, the short cavity length of the VCSOA leads to an inherently large axial mode spacing. Because of this fact, continuous mode-hop-free tuning is achievable over a relatively wide wavelength span. To realize wavelength tuning of the device, we use a MEMS-based optical cavity design similar to that used in tunable VCSELS, RCLEDs and photodetectors. These devices contain a variable-thickness air gap within the resonant cavity structure that allows for variation of the effective cavity length. With a MEMS-tunable vertical-cavity device, there exist a number of distinct optical cavity structures. Here, we will make use of the terminology employed by Larson [25] to outline the relevant optical cavity designs for active devices; these include the semiconductor-coupled cavity (SCC) and extended-cavity (EC) designs. Each design incorporates an air gap within the optical cavity, as described in Fig. 2. By modulating the thickness of this air gap, the resonant wavelength of the cavity may be tuned. For these structures, the suspended mirror will be defined as the membrane DBR and the combination of the membrane DBR and air gap will be referred to as the tunable mirror structure. The top and bottom mirrors are designed to give a π phase shift at the center wavelength of the cavity λ_c, which is defined as the wavelength at which the air gap is of the ideal thickness and the DBRs meet the Bragg condition. For the following, all lengths are given as optical thickness—physical thickness multiplied by the refractive index.

1) SCC Design: The SCC design utilizes a semiconductor cavity containing the active material of length a multiple of $\lambda_c/2$, along with an air gap of thickness near an odd multiple $\lambda_c/4$. In this design, the air gap acts as a low index layer of the top DBR, as seen in Fig. 2(a). The large index step afforded by the air gap allows for enhanced reflectance of the tunable mirror structure, as well as maximum overlap of the optical field with the active region. With the SCC design, the increased optical overlap is achieved at the expense of a decreased wavelength tuning efficiency, resulting in a small wavelength shift for a given change in air-gap thickness. In a tunable vertical-cavity amplifier, the tradeoff of decreased tuning range for increased optical overlap may be preferred, as it is necessary to achieve the highest possible single-pass gain in these devices. In this design, the coupling between the air gap and semiconductor active region leads to complications in the tuning mechanism. These complications include changes in the top mirror reflectance and confinement factor with tuning, which may lead to variations in the peak gain, bandwidth, saturation, and NF over the wavelength tuning range of the amplifier. Depending on the final application, the benefits of the SCC design, including maximum overlap of the optical field with the active material and enhanced top mirror reflectance, may outweigh the resulting tradeoff of a limited tuning response. In addition, the SCC design is simple to implement, as there is no need to access the optical cavity to create the antireflection coating (ARC) necessary in the EC design.

2) EC Design: By placing an ARC within the cavity, at the interface between the semiconductor active region and the variable air gap, the EC structure is produced. Here, the combination of the active region and air gap produces an "extended cavity" of a total thickness of a multiple of $\lambda_c/2$. In this design, the ARC may be fabricated using a simple quarter-wave transformer, with a refractive index value equal to the square root of the active-region refractive index. The EC design allows for increased wavelength tuning ranges when compared to the SCC design, and the tuning response of the EC design is linear, as a function of air-gap thickness, over a relatively wide wavelength range (DBR stop band as well as ARC bandwidth limits the linear tuning range). However, the larger achievable tuning range comes at the expense of reduced optical overlap with the stacked MQW active region. Thus, given a similar active region and mirror design, the EC structure will exhibit reduced peak gain for a given value of material gain, when compared to the SCC structure. Due to the presence of the ARC in the structure, coupled cavity effects are suppressed and more constant gain profiles will result over the wavelength tuning range of the device. Assuming an ideal ARC, the variations in device properties found with tuning will be caused by the wavelength shift of the cavity, as well as those changes brought about by the variation in the total cavity length.

D. Wavelength Tuning

In each of the optical cavity designs described above, the air gap allows for wavelength tuning through the variation in the effective cavity length of the device. Using the modeling approach outlined previously, the tunable mirror structure can be

described using the standard relationships for a FP interferometer [26]. The effective reflectance of the tunable mirror structure may be written as

$$R_{\text{eff}} = \frac{R_c + R_m - 2\sqrt{R_c R_m}\cos(\phi_g)}{1 + R_c R_m - 2\sqrt{R_c R_m}\cos(\phi_g)} \qquad (13)$$

where R_m is the power reflectance of the membrane DBR, R_c is the reflectance of the interface between the semiconductor cavity and the air gap, ϕ_g is the round-trip phase in the air gap $= 2\beta_g L_g + 2(\beta_g - \beta_{go})L_m$, with $\beta_g = 2\pi/\lambda$, $\beta_{go} = 2\pi/\lambda_c$, L_m is the penetration depth into the membrane DBR, and L_g is the thickness of the air gap. Similarly, the reflected phase is given by the relation [25]

$$\phi_{\text{eff}} = \tan^{-1}\frac{\sqrt{R_m}(R_c - 1)\sin(\phi_g)}{\sqrt{R_c}(1 + R_m) - \sqrt{R_m}(1 + R_c)\cos(\phi_g)}. \qquad (14)$$

From (13), we see that the reflectance of the tunable mirror structure varies with the round-trip phase in the air gap. Most notably, with the SCC design the effective reflectance will be reduced with tuning due to phase interference from multiple reflections within the air-cavity structure. When the air gap is near a thickness of an odd multiple of $\lambda_c/4$, the multiple reflections add in phase and result in a maximum in R_{eff}. When the air gap reaches a thickness of a multiple of $\lambda_c/2$, destructive interference occurs and the reflectance reaches a minimum value. With the EC design, the presence of the ARC removes the fixed phase reflection from the bottom of the air gap and, assuming an ideal ARC, $R_c \approx 0$, $R_{\text{eff}} \rightarrow R_m$, resulting in a constant tunable mirror reflectance over the tuning range of the VCSOA, assuming this falls within the stop band of the DBR mirrors and the ARC bandwidth.

Continuing with the FP approach, we may describe the wavelength-tuning characteristics of the SCC design by treating the air gap-DBR structure as a mirror with a tunable phase shift. The resonant wavelength of the optical cavity occurs when the round trip phase of the semiconductor cavity and the DBRs (including the contribution of the air gap in the top mirror) is equal to an integer multiple of 2π. For small changes in L_g centered on the ideal air-gap thickness L_{go}, the shift in wavelength of the resonant cavity mode corresponding to a given change in air-gap thickness is given by [25]

$$\frac{\Delta\lambda}{\lambda_c} = \frac{\gamma_\phi \Delta L_g}{L_b + L_{\text{sc}} + \gamma_\phi(L_g + L_m)} \qquad (15)$$

with the phase coupling factor $\gamma_\phi = d\phi_{\text{eff}}/d\phi_g$. The denominator in (15) describes the total cavity length of the device, including the penetration depth into the bottom DBR L_b, the length of the semiconductor cavity L_{sc}, and the effective length of the tunable mirror structure, which is the sum of the air-gap thickness L_g and the penetration depth into the membrane DBR L_m, scaled by γ_ϕ.

From (15), we find that the wavelength shift of SCC design is directly proportional to the phase coupling factor, thus, for a given change in air-gap thickness, a device with a large γ_ϕ will exhibit a larger wavelength tuning rate. The response of R_{eff}, ϕ_{eff}, and γ_ϕ, as a function of the thickness of the air gap, is shown in Fig. 3. In this plot, it has been assumed that $R_c = 0.32$ and $R_m = 0.95$. With these values, γ_ϕ exhibits a minimum
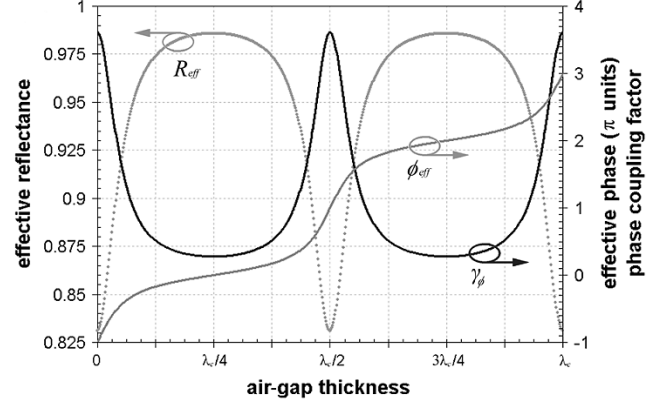

Fig. 3. Effective mirror reflectance, reflected phase, and phase coupling factor of the SCC design as a function of the thickness of the air gap, with $R_c = 0.32$ and $R_m = 0.95$.

value of about 0.28 when the air-gap thickness is equal to an odd multiple of $\lambda_c/4$. In this case, any change in the air-gap thickness will result in a change in the effective cavity length that is scaled by the value of the phase coupling factor. Within this linear tuning regime, the small value of the phase coupling factor reduces the effects of tilt or additional loss that may be caused by nonuniformity of the membrane DBR, by reducing the total penetration depth of the optical field into the tunable mirror structure. However, for large membrane displacements, the phase coupling factor will increase dramatically, reaching a maximum value of 3.61 at integer multiples of $\lambda_c/2$. For the EC design, if we assume that the active region–air interface contains an ideal ARC, γ_ϕ becomes unity in (15) and the tuning response is directly related to the change in air-gap thickness; note that this linear tuning regime for the EC structure will be limited by the finite width of the DBR stopband, as well as the bandwidth of the ARC. Because of the increase in γ_ϕ as compared to the SCC design, the EC structure is more sensitive to imperfections in the membrane DBR.

E. Signal Gain of MEMS-Tunable VCSOAs

From the relationships presented above, it is possible to derive expressions describing the effects of the tunable mirror structure on the peak gain of the VCSOA. Combining (1) for the peak reflection gain (with $\phi_s = 0$), with the relationships describing the reflectance of the tunable mirror structure (13), the peak signal gain of a reflection mode SCC-design tunable VCSOA may be written as

$$G_r = \frac{(\sqrt{R_{\text{eff}}} - g_s)^2}{(1 - \sqrt{R_{\text{eff}}}g_s)^2} \qquad (16)$$

where we have assumed that the device contains a highly reflective fixed mirror $(R_b = 1)$ and a slightly transmissive membrane DBR $(R_m < 1)$. This expression shows that the peak gain is dependent on the effective reflectance of the tunable mirror structure, which is a function of the membrane reflectance, the cavity–air interface reflectance and the round trip phase of the air gap.

Another option for the SCC-design reflection-mode tunable VCSOA would be to use the tunable mirror structure as the highly reflective mirror. In the limit of $R_m = 1$ in (13), $R_{\text{eff}} \rightarrow$
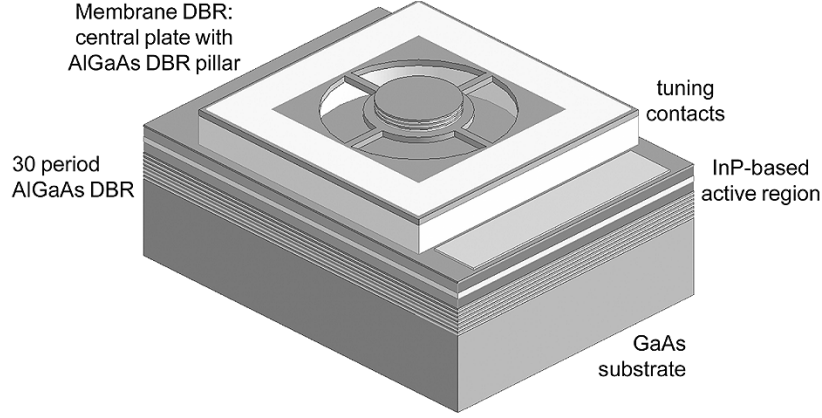
Fig. 4. Three-dimensional schematic of the MT-VCSOA, highlighting the four-leg design of the suspended DBR structure. With an applied voltage the membrane DBR is attracted toward the substrate, reducing the air-gap thickness, and resulting in a blue shift of the VCSOA cavity mode.

1 regardless of the round-trip phase of the air gap, and the expression for the peak gain is given by

$$G_r = \frac{(\sqrt{R_t} - g_s)^2}{(1 - \sqrt{R_t}g_s)^2} \qquad (17)$$

where R_t is the transmissive mirror in this case. Thus, by using the MEMS tuning structure as the highly reflective mirror in the reflection-mode SCC—design VCSOA, the peak gain relationship becomes independent of both the reflectance of the cavity–air interface and the round-trip phase of the air gap. In this configuration, the MEMS-tuning element may be described as a Gires–Tournois interferometer, which is essentially an FP interferometer with a unity back reflector. This same expression can be used to model the reflection mode EC-design tunable VCSOA. The incorporation of an ideal ARC results in $R_c \approx 0$ and the peak gain in reflection mode for both mirror positions reduces to that shown in (17), where R_t will be the reflectance of the transmissive mirror, regardless of position (again assuming the highly reflective mirror has unity reflectance).

With a transmission-mode VCSOA, the need for two transmissive mirrors requires that both R_m and $R_b < 1$. Combining (2) with (13), the peak gain for a transmission mode SCC-design VCSOA becomes

$$G_t = \frac{g_s(R_b - 1)(R_{\text{eff}} - 1)}{(1 - \sqrt{R_b R_{\text{eff}}}g_s)^2}. \qquad (18)$$

With this configuration, the peak transmission gain is dependent on the reflectance of the cavity–air interface and both DBRs, as well as the round-trip phase in the air gap. The changing mirror reflectance with tuning described by (13) may be suppressed by employing the EC structure in these devices. Again, assuming an ideal ARC($R_c \approx 0$), the peak gain for a transmission-mode VCSOA using the EC design reduces to the standard expression as seen in (2), with the membrane mirror reflectance R_m replacing either the top or bottom mirror reflectance, depending on the configuration of the structure.

III. ELECTROSTATIC ACTUATION

To achieve wide wavelength tuning of the VCSOA cavity mode, it is necessary to construct a mechanical system to physically alter the thickness of the air gap. The most efficient realization of such a structure involves the use of an integrated micromechanical actuator. Depending on the configuration of the actuator, the air-gap thickness may be increased or decreased from its initial position. With an increase (decrease) in the air-gap thickness, the effective cavity length is increased (decreased) and the cavity resonance wavelength is red (blue) shifted, as can be seen in (15). Using a MEMS-based tuning element, various actuator designs are possible; the most commonly used being electrostatic and thermal actuators. A schematic of the MT-VCSOA is included as Fig. 4.

For a low-power high-speed tuning response, the most effective actuator design is the integrated electrostatic actuator. In its simplest form, the electrostatic actuator consists of a pair of parallel capacitor plates separated by an air gap of a specified thickness, in which one or more of the plates is freely suspended. With an applied bias, the Coulomb force is exerted on the plates due to the charge separation present. If one, or both, of the plates is free to move, then the electrostatic force results in a change in the air-gap thickness, leading to a variation in the effective cavity length of the VCSOA. Because the air gap is an integral part of the resonant cavity, the thickness will be constrained by the optical design of the device. Neglecting the effects of fringing fields (lateral dimensions $\gg$ air-gap thickness) and assuming that the device consists of a rigid central plate suspended by a set of four deflectable legs, with no intermediate insulating layers between the two electrodes, the resulting force F_c may be calculated from [27]

$$F_c = \frac{\varepsilon_o A_m V^2}{2(L_{g_o} - \delta_m)^2} + \frac{2\varepsilon_o b l V^2}{L_{g_o}(L_{g_o} - \delta_m)} \qquad (19)$$

where ε_o is the permittivity of free space, A_m is the total plate area, V is the applied bias, L_{g_o} is the initial separation between the plates of the actuator, δ_m is the vertical displacement of the suspended plate, l is the length of the individual legs, and b is the leg width. In (19), the first term represents the force distributed across the central plate, while the second term represents the force generated along the length of the legs, assuming a linear deflection as a function of the lateral dimension.

With the applied force known, as a first approximation, the deflection of the compliant MEMS structure may be described using Hooke's law, $F_c = F_{\text{restore}}$, with a simple one-dimensional model for the restoring force of the actuator $F_{\text{restore}} =$

$k_{\mathrm{mech}}\delta_m$, where k_{mech} is the mechanical spring constant of the actuator. Because the electrostatic force itself is a function of the displacement, an iterative solution must be used to determine the equilibrium deflection of the actuator. More advanced modeling techniques to describe the mechanical properties of the MEMS structure include the area-moment method [28] or full three-dimensional (3-D) models using finite-element analysis [29]. However, it has been found that, by using analytical formulas such as those presented here, accurate predictions of the mechanical properties of the actuator can be made.

For our simple one-dimensional (1-D) model, the restoring force may be described by utilizing the familiar relationships of the flexure of beams of uniform cross section [30]. The total restoring force of the mechanical system can be found by summing the forces resulting from bending and stretching of the beam, as well as the force present due to intrinsic stress present in the legs. In this case, the components of the restoring force of four cantilever-like tethers loaded at their tips by a rigid center-loaded section can be shown to be [31]

$$F_{\mathrm{stress}} = \frac{\pi^2 hb\sigma\delta_m}{2l} \quad F_{\mathrm{bend}} = \frac{\pi^4 E'h^3b\delta_m}{24l^3}$$
$$F_{\mathrm{stretch}} = \frac{\pi^4 E'hb\delta_m^3}{32l^3}. \tag{20}$$

In this expression, h is the thickness of the legs, E' is the biaxial modulus with $E' = E/(1-v^2)$, E is the Young's modulus of the membrane material, v is Poisson's ratio, and σ is the intrinsic film stress in the beam. With these expressions, the mechanical spring constant k_{mech} may be found by dividing F_{restore} by the membrane deflection δ_m. It should also be noted that the relationships above are valid only for uniform beams. For a composite actuator consisting of two distinct films, the modulus, thickness, and stress must be replaced by the effective values for a bilayer [32]. Given a very thin structure fabricated from materials with a high intrinsic film stress value, the restoring force will be dominated by the first term F_{stress}. In those structures in which the growth stresses have been minimized, or in structures with a relatively large cross-sectional area, such as a device with a full thickness DBR as the compliant structure, the restoring force will be dominated by the bending of the legs. F_{stretch} becomes important at large displacement values; however, this term is usually insignificant in tunable vertical-cavity devices. As compared to a cantilever, the four-leg design is a more mechanically stable structure. In this configuration, the sensitivity of the free-standing membrane to external mechanical vibrations and stress-induced bending in the structural films may be reduced [33]. In addition, the four-leg design helps to maintain a parallel alignment between the membrane DBR and fixed substrate DBR, thus reducing the effects of beam walkoff loss upon actuation [27].

The displacement of the electrostatic actuator is highly nonlinear, due to the changing force with displacement, as seen in (19). Due to this inherent nonlinearity, the electrostatic actuator will only exhibit a limited range of valid solutions. As a rule of thumb, for displacements less than $1/3$ of the initial air-gap thickness, there exists a stable equilibrium position for the actuator. Beyond this distance, the electrostatic force overwhelms the restoring force and leads to pull-in of the actuator. At this
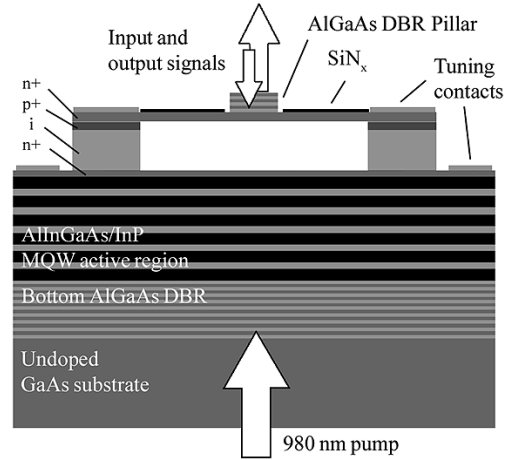

Fig. 5. Cross-sectional schematic of the wafer-bonded long-wavelength MT-VCSOA. The device operates in reflection mode and is pumped with a 980-nm laser; wavelength tuning is achieved with the SCC tunable cavity design.

point, the membrane will be forced into physical contact with the opposite electrode, resulting in a permanent fusing of the pair due to the effects of stiction or damage due to capacitive discharge if there are no insulating materials separating the electrodes. A review of the intricacies of the electrostatic actuator may be found in [34]. Using this rule of thumb as a limit to the total travel of the actuator, it is possible to estimate the maximum voltage for the four-leg design. Setting the relevant cases in (20) equal to the applied force in (19), and solving for the required voltage for a displacement of $1/3L_{go}$, we find

$$V_{\mathrm{stress}}^{\max} = \frac{2\pi}{3}\left(\frac{hb\sigma L_{go}^3}{\varepsilon_o l(3A_m + 8bl)}\right)^{1/2}$$
$$V_{\mathrm{bend}}^{\max} = \frac{\pi^2}{3}\left(\frac{h^3 bE'L_{go}^3}{3\varepsilon_o l^3(3A_m + 8bl)}\right)^{1/2}. \tag{21}$$

For both of these expressions, the voltage may be reduced by increasing the length of the legs and the area of the membrane, as well as decreasing the initial air-gap thickness. Specific to the stress-dominated structure, the required tuning voltage may be minimized by decreasing the cross-sectional area of the legs (hb) and the film deposition stress. For the case where F_{bend} dominates, the required voltage is largely dependent on the thickness and length of the legs. Because the suspended structure serves as the top mirror for the device, the thickness of the legs will be predetermined by the optical design of the DBR, although additional processing steps may be used to decouple the mechanical and optical properties of the device, allowing increased freedom in the design of the final structure [35].

IV. DEVICE STRUCTURE AND FABRICATION

A schematic of the cross section of the MT-VCSOA is shown in Fig. 5. This structure is the same as that presented in [9]. The MT-VCSOA utilizes an InP-based active region that is bonded to two AlGaAs DBRs via a direct wafer bonding procedure [36]. By using wafer bonding, it is possible to combine the high-gain long-wavelength InP-based active material, with the excellent

thermal properties and high index contrast of AlGaAs-based DBRs. The active region consists of a stacked MQW structure, containing five sets of five compressively strained AlIn-GaAs QWs placed at the peaks of the standing optical wave in a $5\lambda_c/2$ cavity, with the peak gain designed to be at 1545 nm at room temperature. The InP-based active material is grown by metal–organic chemical vapor deposition (MOCVD), while the DBRs are grown using molecular beam epitaxy (MBE). The bottom mirror is a 30-period GaAs–Al$_{0.98}$Ga$_{0.02}$As DBR with a calculated reflectance of 0.999, while the top DBR consists of either four or five periods of GaAs–Al$_{0.98}$Ga$_{0.02}$As on top of a $3\lambda_c/4$ n$^+$ GaAs layer, a $5\lambda_c/4$ (optical thickness in air) Al$_{0.98}$Ga$_{0.02}$As sacrificial etch layer, and a $\lambda_c/4$ n$^+$ GaAs layer directly above the active region. This structure forms the SCC-design tunable DBR, which includes the air gap as a low index layer. The peak reflectance of the top mirror structure is calculated to be 0.968 for four periods on top of the GaAs structural layer and 0.976 for five periods, including the contributions of the air gap as a low index layer. As grown, the Al-GaAs top mirror wafer contains a five-period DBR on the GaAs membrane layer; during the fabrication procedure one period is removed using a wet chemical etching process to create the four-period devices. The MT-VCSOA is designed to be pumped optically with a 980-nm diode laser and to operate in reflection mode.

As shown in the schematic, the GaAs membrane and the $\lambda_c/4$ GaAs layer closest to the active region are doped n$^+$. The sacrificial AlGaAs layer is comprised of 200 nm of p$^+$ Al$_{0.98}$Ga$_{0.02}$As, followed by 1750 nm of intrinsic Al$_{0.98}$Ga$_{0.02}$As. A reverse bias across this n$^+$/p$^+$/i/n$^+$ diode creates an electrostatic force that results in the displacement of the membrane toward the substrate. With this actuator design it is only possible to reduce the air gap, thus it is only possible to blue shift the resonant wavelength of the VCSOA. With the doping scheme described here, the tuning diode is designed to have a reverse breakdown voltage of 60 V. During the fabrication procedure a thin layer of tensile-stressed (260 MPa) SiN$_x$ is deposited on top of the membrane and legs. This film creates a slight tensile stress in the structure to ensure the flatness of the free-standing membrane.

The basic fabrication procedure for this device may be found in the literature [9]. However, for the revised mechanical design presented here, an additional liftoff step is added prior to release in order to constrain the free edges of the mechanical support structure and avoid excessive undercutting of the sacrificial layer below the supports [37]. For the liftoff procedure, a low-temperature (100 °C) SiO$_2$ layer is deposited using inductively coupled plasma-enhanced chemical vapor deposition (PECVD), as demonstrated in Fig. 6. Additional changes include a radiused support structure, in order to reduce the effects of stress concentration, and an enlarged DBR pillar to increase the rigidity of the central portion of the membrane.

V. EXPERIMENTAL RESULTS

A. Testing Procedure

In order to facilitate the mechanical analysis of the MEMS tuning structure, the initial air-gap thickness is measured using
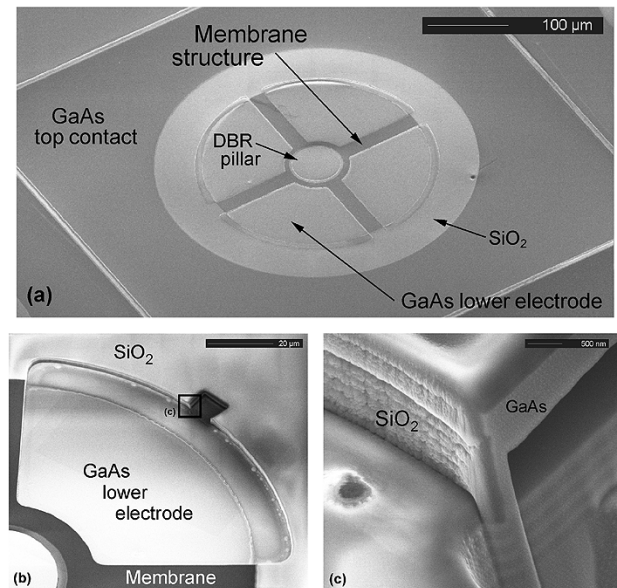

Fig. 6. Scanning electron micrographs of the updated tunable VCSOA mechanical design. (a) Here a low-temperature SiO$_2$ film has been patterned by liftoff to reduce excessive undercutting of the sacrificial material below the support structure. (b) A small via has been cut into the sidewall using a focused ion beam in order to examine the sidewall coverage of the SiO$_2$ film. (c) Close-up of the highlighted area in (b); note that the SiO$_2$ film exhibits conformal sidewall coverage.

a vertical-scanning interferometer, and the displacement of the membrane DBR is recorded using a laser Doppler vibrometer. For optical testing, an external-cavity tunable laser diode operating near 1550 nm is used as a signal source, while the input signal power is controlled by a variable optical attenuator to be −35 dBm. In all tests presented here, the amplifier is operated below saturation. As the device is operated in reflection mode, the signal is coupled into and out of the top of the device through a fiber focuser, and a circulator is necessary to separate the amplified output. A 980-nm laser, which is coupled in through the bottom DBR by another fiber focuser, serves as the optical pump. The use of optical pumping allows for the generation of a uniform carrier distribution given the large number of QWs. An optical spectrum analyzer is used to record the characteristics of the VCSOA as a function of pump power, tuning bias, and wavelength. By recording the individual gain spectra as a function of wavelength, and fitting the data with (1), the variation in peak gain, top mirror reflectance, and single-pass gain may be determined over the wavelength span of the tunable VCSOA. With these devices, the tuning range is recorded by noting the wavelength of the amplified spontaneous emission (ASE) peak as a function of the applied bias to the electrostatic actuator. The signal coupling loss for this experiment is measured to be about 7 dB.

B. Wavelength Tuning

With the MT-VCSOA, the decrease in air-gap thickness upon actuation leads to a reduction in the effective cavity length, and a blue shift in the peak gain wavelength. For the SCC design, the competing phases from the multiple reflections present in the air-cavity structure lead to a varying phase coupling factor (Fig. 3) and a nonlinear wavelength shift with respect to the
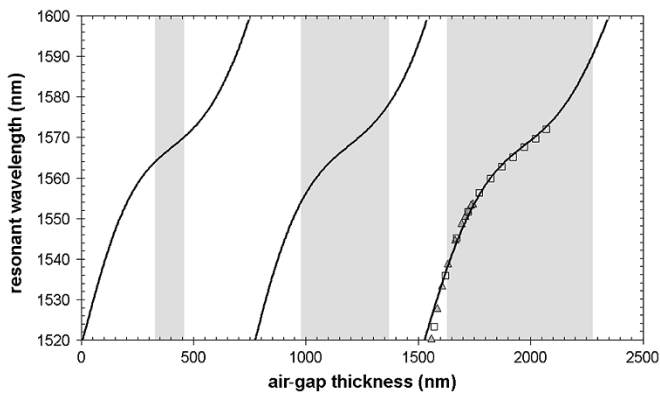
Fig. 7.   Wavelength shift as a function of the air-gap thickness for L_g centered on $\lambda_c/4, 3\lambda_c/4$, and $5\lambda_c/4$. The shaded regions indicate the estimated wavelength tuning range given the limited travel of the electrostatic actuator, while the open squares and triangles represent experimental data from devices with the widest tuning ranges.
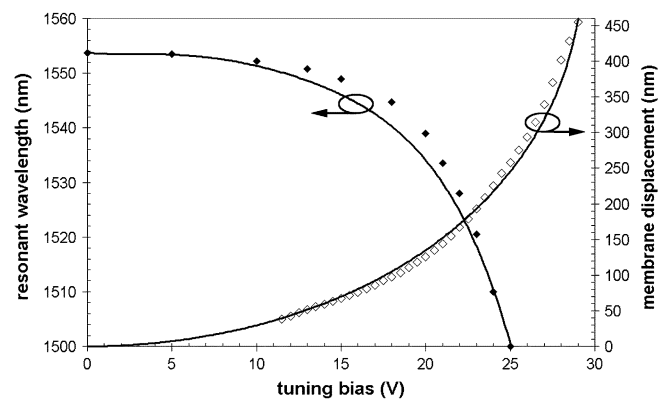

Fig. 8.   Resonant cavity mode shift as a function of the applied tuning bias, as well as the corresponding membrane displacement. The solid lines indicate the theoretical device response, while the data points indicate experimental measurements.

change in air-gap thickness, as seen in Fig. 7. In this plot, the tuning response for a $\lambda_c/4, 3\lambda_c/4$, and $5\lambda_c/4$ air-gap structures are presented, as well as measured data from our MT-VCSOA. Using this plot, it is possible to compare the maximum tuning range around the center wavelength of the cavity λ_c, given the limited travel of the electrostatic actuator [38]. Assuming that the displacement is limited to $\sim 1/3 L_{go}$ and centered at λ_c, the approximate wavelength shift for each structure is found to be 6.4 nm for the $\lambda_c/4$ air gap, 24.2 nm for the $3\lambda_c/4$ air gap, and 53.1 nm for the $5\lambda_c/4$ air gap. For the cavity designs presented in Fig. 7, the estimated wavelength tuning range is highlighted as the shaded area of the plot. By increasing the air-gap thickness, the total wavelength tuning range may be extended. However, with an increasing air-gap thickness, the required tuning voltage will also increase due to a decrease in the applied force from (19). Additionally, given a longer total cavity length, the FP mode spacing is reduced, decreasing the overall single-mode tuning range.

Using the same basic cavity structure, we can also predict the wavelength tuning response for the EC design. In the limit of an ideal ARC, $R_c \approx 0$ and $\gamma_\phi \to 1$. With this design, the resonant wavelength shift becomes linear as a function of the change in air-gap thickness (not taking into account dispersion effects in the DBRs or ARC bandwidth). Again, using air-gap thicknesses centered around $\lambda_c/4, 3\lambda_c/4$, and $5\lambda_c/4$, the limits to the wavelength shift are found to be 15.8, 44.6, and 70.5 nm, respectively. Thus, by incorporating an ARC within the cavity, the wavelength tuning range of the VCSOA may be increased. On the other hand, the extended tuning range comes at the price of a reduced optical overlap with the stacked MQW active region, resulting in a reduced signal gain for a given pump power.

For the measured data, the ASE wavelength tuning range is greatly extended as compared to the previous generation of devices. In this case, the revised mechanical structure results in a slightly reduced initial air-gap thickness and an initial cavity mode with a shorter wavelength than desired. Upon tuning, the phase coupling factor begins to increase dramatically, and the wavelength shift becomes very rapid with decreasing air-gap thickness. The results for the two most widely tunable devices

are included in Fig. 7. With these devices, the ASE wavelength shifts are 76.6 nm (1571.9 nm to 1495.3 nm) with the application of 30 V to the tuning diode and 53.8 nm (1553.8 nm to 1500.0 nm) at 25 V. Due to the reduced initial air-gap thickness, the experimental tuning data is blue shifted with respect to the ideal design, resulting in measured data points that extend beyond the limit of the wavelength tuning range indicated in the figure. For both the four- and five-period samples, the wavelength response is effectively identical; at the furthest extent of the tuning range, the deviation between each case is less than a nanometer.

Apart from the physical limitations of the mechanical structure, the useful wavelength span of the MT-VCSOA will eventually be limited by either the finite stop band of the DBR mirrors or the gain spectrum of the active material. Wide mirror stop bands may be achieved through the use of air/semiconductor DBRs [18], [37], oxidized AlGaAs DBRs [39], or dielectric DBRs [15]. In addition to the increased stopband width, the increased index contrast with these mirror systems leads to a smaller penetration depth and thus an increase in the wavelength tuning efficiency, due to a decrease in the overall cavity length. Given an infinite DBR stopband and an actuator capable of an extended range of displacement, the wavelength range over which acceptable amplification may be achieved will be limited by the active material gain spectrum.

C. Mechanical Analysis

With the updated mechanical structure, the total membrane displacement is improved, while at the same time the required operating voltage is largely reduced, as compared with the previously reported devices in [9]. As seen in Fig. 8, with a plate diameter of 70 μm, a spring length and width of 95 μm and 20 μm, respectively, a membrane thickness of 0.35 μm, and SiN$_x$ thickness of 0.25 μm, we have achieved a total displacement of 455 nm with the application of 29 V to the tuning diode. With this actuator, the application of 25 V results in a membrane displacement of approximately 250 nm and a corresponding ASE wavelength shift of 53.8 nm, as shown in Fig. 8. The large decrease in the required tuning voltage may be attributed to the better control over the air-gap thickness found

with the new actuator design. With the previous mechanical design, the deformation of the support structure caused the air gap to nearly double in thickness [9]. By constraining the support structure against out-of-plane deformation, the initial plate separation is now better controlled, leading to a large reduction in the required tuning voltage for the revised mechanical design.

Combining (19) with the sum of the components of the restoring force from (20) and using an iterative solution, it is possible to accurately predict the displacement of the membrane structure as a function of the applied bias. Fitting the theoretical curve to the measured values as shown in Fig. 8, the spring constant of the actuator is found to be 58.6 N/m. This value is relatively high due to the large tensile stress in the PECVD SiN$_x$ layer. The mechanical spring constant is dominated by the material stress term $k_{\text{stress}} = 56.1$ N/m, while the bending and stretching components contributes only slightly to the restoring force, with $k_{\text{bend}} = 2.2$ N/m and $k_{\text{stretch}} = 0.3$ N/m at a displacement of 247 nm. To minimize the total restoring force of the actuator and further reduce the required tuning voltages, a low, or ideally zero, tensile stress actuator material should be used, similar to that demonstrated in [40]. Presently, a more thorough understanding of the stresses developed by the direct wafer bonding process is necessary in order to optimize the mechanical properties of the actuator.

D. Mirror Reflectance

From (13), we see that the use of MEMS-based wavelength tuning results in varying mirror reflectance as a function of the round-trip phase of the air gap (ϕ_g). With both reflection and transmission mode VCSOAs, the mirror reflectance is crucial in determining the characteristics of the amplifier, including the gain, bandwidth, saturation, and noise figure [10]–[12]. With the SCC design, the varying reflectance is caused by the changing magnitude of interference from the multiple reflections within the air-cavity structure. At the center of the tuning range, the air gap is near a point of antiresonance ($\sim\lambda_c/4$), and the multiple reflections add in phase, leading to a peak in the effective reflectance. However, as L_g is varied, the air-gap thickness begins to approach a multiple of $\lambda_c/2$, in this case scaled by the effective index of the cavity, which is a combination of the air gap and semiconductor active region, eventually reaching a position where the reflection from the suspended DBR and semiconductor–air gap interface are 180° out of phase, resulting in a minimum in the effective mirror reflectance. From the perspective of the semiconductor cavity, the destructive interference leads to a reduced effective mirror reflectance as the air-gap thickness is deviated from its ideal value.

Combining (13) and (15), it is possible to plot the effective reflectance of the SCC air gap-DBR structure as a function of the resonant wavelength of the VCSOA, as shown in Fig. 9. In this plot, we have used $R_c = 0.32$, and we are assuming that the center wavelength of the tunable mirror structure is the same for all devices. Because the experimental data were recorded for different samples, slight nonuniformities in the epitaxial growth procedure may shift the ideal value of λ_c for each device. Along with the theoretical curves, we have included the data collected by curve fitting the gain spectra using (1) for samples with four- and five-period DBR pillars. For the four-period DBR pillar, the
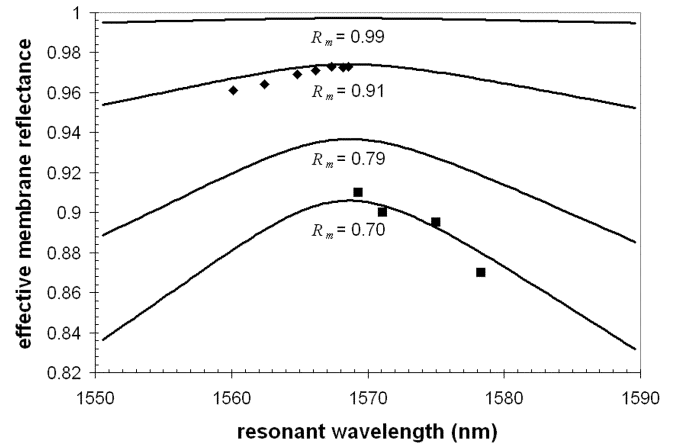

Fig. 9. Theoretical curves for the variation in reflectance of the membrane DBR structure with the SCC design. Experimental data recorded for both four- and five-period devices are included.

measured peak reflectance value is 0.91 at 1569.3 nm and drops to 0.87 at a wavelength of 1578.3 nm. In this device, the measured maximum reflectance is much lower than the theoretically calculated peak value of 0.968 and is attributed to additional mirror loss brought about by the wet chemical etching process used to remove one of the mirror periods [1]. For the five-period sample, the peak R_{eff} of 0.974 matches well with a predicted value of 0.976. With increasing peak mirror reflectance, the roll off in R_{eff} becomes much less severe. With roughly 20 nm of tuning from the peak reflectance wavelength, the theoretical reflectance drops to 0.953 at 1550 nm for the five-period structure.

Also included in Fig. 9 is the variation in mirror reflectance for a typical SCC-design MEMS-tunable VCSEL with a peak effective reflectance of 0.997 for the tunable mirror structure [27]. Over the same wavelength range, R_{eff} reduces only slightly to 0.995. If we examine the limit of top mirror reflectance $R_m = 1.00$, then the effective top mirror reflectance reduces to unity and becomes independent of the phase detuning of the air gap. Over the wavelength tuning span of the VCSOA, the variation in reflectance of the membrane DBR structure may be extremely large with the SCC design. As compared with the mirror requirements in a VCSEL, the lower reflectance values necessary with the VCSOA lead to a much larger change in mirror reflectance as the air gap is varied from its ideal thickness. In this case, the roll-off in reflectance will greatly diminish the wavelength span over which acceptable amplification may be achieved.

E. Signal Gain

Using the relationships developed in Section I to describe the peak gain of the various tunable VCSOA configurations (16)–(18), it is possible to model the response of the amplifier as a function of the cavity resonance wavelength. In order to complete this model, the wavelength dependence of the single-pass gain g_s must be determined. As the cavity mode is tuned, the VCSOA will operate at different points along the material gain curve, leading to changes in g. Additionally, the wavelength shift will lead to a translation of the standing wave peaks within the active region. As a result, the position of the maximum field
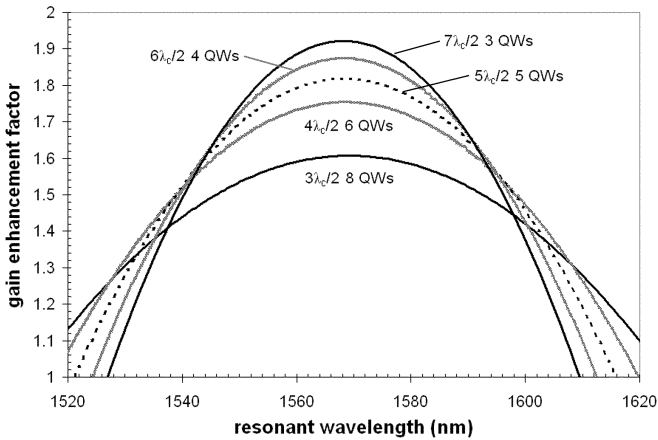
Fig. 10. Variation in gain-enhancement factor of the SCC tunable cavity design for various cavity lengths and MQW designs.
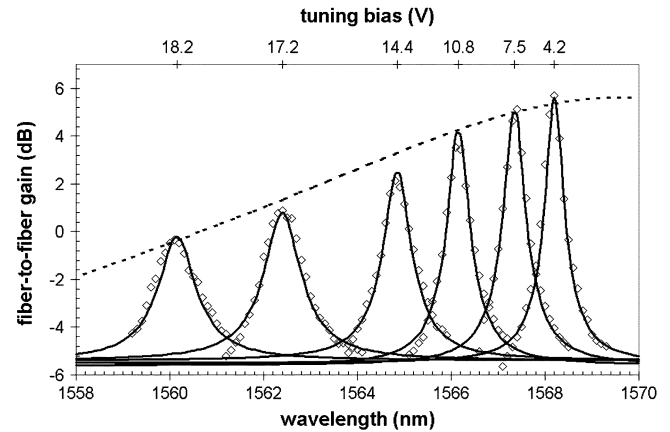

Fig. 11. Amplifier gain spectra recorded for a constant pump power and increasing tuning bias (open circles). Fitting the experimental gain spectra (solid lines) with the expression from (1), the variation in single-pass gain and mirror reflectance may be determined. Using these parameters, it is possible to generate curves describing the peak signal gain as a function of the cavity resonance wavelength (dashed line).

intensity will sweep across the MQW stack, leading to a varying gain-enhancement factor with tuning. In terms of the cavity loss (product of $\alpha_i L_c$), the deflection of the membrane structure may lead to increased losses caused by tilting or nonuniform deformation of the released structure; however, for the model presented here, we have assumed that the product $\alpha_i L_c$ remains constant over the wavelength tuning range. Here we have used an average cavity loss of about 35 cm^{-1}. This value is relatively high compared to nontunable vertical-cavity devices and is attributed to the doping levels used in the electrostatic actuator structure, the presence of multiple wet-etched semiconductor-air interfaces within the cavity, and increased diffraction loss associated with the longer cavity. Next, g and ξ must be determined over the wavelength span of the tunable VCSOA.

In order to estimate the change in ξ, a transmission matrix solver (VERTICAL) was used to determine the position of the standing wave peak as a function of the cavity resonance wavelength. For this calculation, the QW structure consists of a given number of 5.5-nm-thick wells separated by two 9-nm barriers (each MQW stack begins and ends with a layer of barrier material). The optical cavity utilizes the SCC design with a $5\lambda_c/4$ air gap. The calculation is completed for cavity lengths of $3\lambda_c/2, 4\lambda_c/2, 5\lambda_c/2, 6\lambda_c/2,$ and $7\lambda_c/2$, containing eight, six, five, four, and three wells per MQW stack. With the transmission matrix solver, the shift in position of the standing wave peaks was recorded as a function of the cavity resonance wavelength. The peak shift is relatively linear as a function of wavelength, and the rate of the spatial shift increases with increasing cavity length. For the cavity lengths presented above, the average shift in position of the standing wave peaks are 0.98, 1.07, 1.16, 1.24, and 1.33 nm per nm of wavelength tuning, respectively.

From the results in Fig. 10, it is possible to see that, with the shorter cavity length designs, the larger required L_{MQW} results in a reduced initial value of ξ; however, the change in ξ becomes less pronounced as the device is tuned from λ_c. With an increased cavity length and a smaller number of wells per stack, the initial enhancement is increased, but the roll-off in ξ becomes more severe with tuning. Assuming a 50-nm wavelength tuning range centered on λ_c (approximately 1570 nm for

this model), the largest variation in enhancement occurs for the $7\lambda_c/2$ cavity. In this structure, ξ varies by approximately 23%, from a maximum value of 1.92 at λ_c nm to minimum of 1.56 after a blue shift of 25 nm from the peak wavelength. Within the approximately 50-nm achievable tuning range, a longer cavity with fewer wells per stack will result in a larger value of ξ. However, if the tuning range is extended or if the device operates off of the ideal center wavelength (λ_c), a larger L_{MQW} may be desired in order to ensure that ξ stays sufficiently high over the wavelength span of the device.

With the variation in ξ established, the final parameter to be determined is the material gain spectrum. By recording the individual amplifier gain spectra for various tuning bias values (at a constant pump power) and fitting the data with theoretical curves generated from (1), it is possible to extract the changes in mirror reflectance and single-pass gain g_s with tuning. An example of this procedure may be seen in Fig. 11. Given the variation in g_s, the material gain as a function of wavelength can be calculated from (4). In this model, no wavelength-dependent losses have been assumed. After backing out the material gain values, it is found that the roll off in g near the gain peak may be well approximated by a Lorentzian function. Such an approximation is a valid first approach for modeling of the material gain spectrum [22]. With the wavelength dependence of g determined, the signal gain response of the tunable VCSOA can be described using the FP amplifier expressions.

By varying the applied bias on the electrostatic actuator, the narrow gain spectrum of the VCSOA may be swept over the wavelength tuning range of the device. With increasing voltage, the resonant wavelength, and thus the position of peak gain, is pushed to shorter wavelengths. Here both the gain bandwidth and peak gain vary over the tuning range due to the changes in g_s and R_{eff} found in our reflection mode SCC-design tunable VCSOA. In order to facilitate a more general comparison of the signal gain characteristics of the various tunable VCSOA configurations, it is desirable to decouple the properties of the MEMS actuator design. Rather than plotting the variation in gain with applied bias, a more general description involves
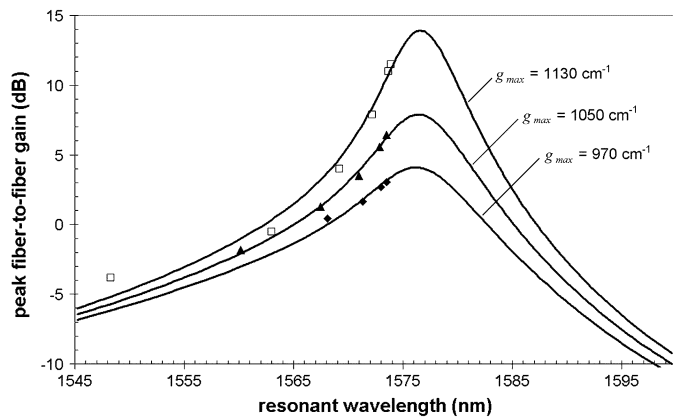
Fig. 12. Theoretical and experimentally measured peak fiber-coupled gain as a function of the resonant cavity wavelength of the VCSOA. The theoretical curves are generated from (16), after matching the wavelength tuning response in (15).
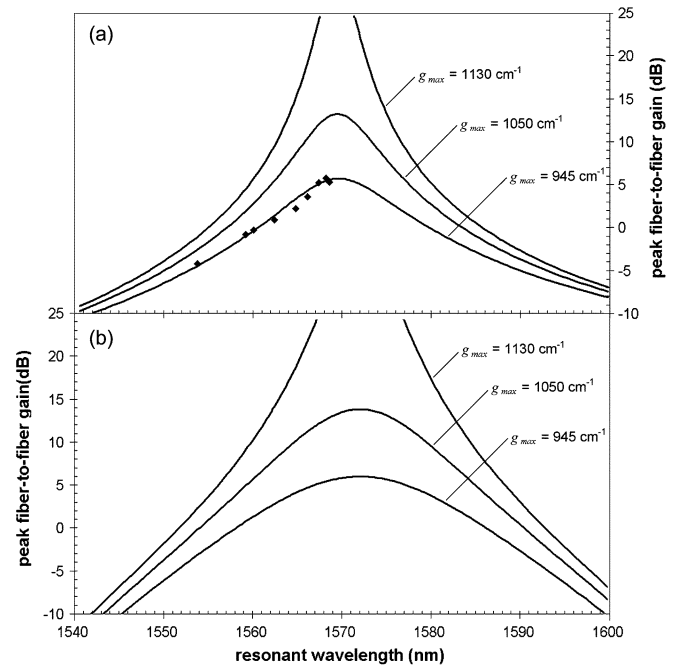

Fig. 13. Theoretical peak fiber-coupled gain as a function of the resonant cavity wavelength for our standard design compared with experimental data (a), and for the inverted SCC-design reflection mode VCSOA (b), with the membrane DBR used as the highly reflective mirror.

the use of the peak gain expressions for the tunable VCSOA (16)–(18). Using these relationships, the variation in peak gain may be plotted as a function of the resonant wavelength of the optical cavity. The peak gain curves generated from these relationships may be described as the envelope function of the individual gain spectra; an example of this can be seen as the dashed curve in Fig. 11.

By recording the peak signal gain for a number of different pump powers, as a function of the resonant wavelength of the VCSOA, a family of gain-tuning curves may be generated. An example of this is shown in Fig. 12 for our SCC-design tunable VCSOA. The theoretical signal gain curves assume a constant value of pump power over the device tuning range. For each pump power, the peak value of material gain is labeled in order to facilitate a more general comparison of the device results, independent of the pumping method. The theoretical curves have been generated using the appropriate peak gain expression from Section II; in this case, (16) is used for the reflection-mode SCC-design tunable VCSOA. Additionally, this model includes all previously described parameters including the wavelength response as a function of L_g, the variation in mirror reflectance, and the change in gain enhancement with tuning. It is important to note that heating effects are not taken into account here.

For the device presented in Fig. 12, the tunable mirror reflectance peaks near 1575 nm, while we have achieved the best fit with the material gain peak at 1572 nm. The position of the material gain peak agrees with the theoretically expected value for our active region. Here the photoluminescence peak is designed to be at 1545 nm at room temperature, leading to a peak gain wavelength near 1550 nm. Assuming the wavelength of peak gain red-shifts at a rate of 0.5 nm/K [6] and given a temperature rise of roughly 40–50 K in the MQW structure with the pump powers used in testing, we would expect to see a red shift of the theoretical peak gain to wavelengths between 1570–1575 nm. In this device, the offset in the peak reflectance of the tunable mirror structure and the peak material gain wavelength leads to an asymmetric peak gain response over the device tuning range. Additionally, the position of peak gain is found to correspond with the wavelength of peak mirror reflectance. The maximum-recorded fiber-to-fiber gain is 11.5 dB

at a pump power of 100 mW (corresponding to a peak material gain of 1130 cm^{-1} in Fig. 12) and 3-dB chip gain, neglecting coupling losses, is recorded over a 25.6-nm wavelength range (1548.3–1573.9 nm). At 100 mW of pump power, at least 3-dB fiber-to-fiber gain (including 7 dB of signal coupling loss) is recorded from roughly 1568 to 1574 nm. With increasing pump power, the device achieved lasing action near the peak of the tunable mirror reflectance. Since it is only possible to blue shift the resonant wavelength of the VCSOA, we are unable to record signal gain values for wavelengths longer than about 1574 nm, which is the initial resonant wavelength of the device. Based on these results, we can verify that our model matches the recorded experimental data. Going one step further, it is possible to model the peak gain response of the MT-VCSOA given arbitrary cavity and mirror designs.

In the first model, we use a reflection-mode VCSOA with an SCC-tunable cavity design, a $5\lambda_c/2$ semiconductor cavity (containing the same stacked MQW active region used in our fabricated devices), a $5\lambda_c/4$ air gap, $R_m = 0.91, R_c = 0.32, R_b = 0.999$, and assuming a signal coupling loss of 7 dB. This model is similar to that shown previously; however, here the peak reflectance of the tunable mirror structure occurs much closer to the gain peak. The theoretically generated peak fiber-to-fiber gain curves are shown in Fig. 13(a). Also included with the theoretical curves is experimental data recorded for a sample exhibiting a peak mirror reflectance near 1570 nm (material gain peak is again assumed to be at 1572 nm for all examples). With this design, the theoretical wavelength span over which 10 dB of fiber-to-fiber gain may be achieved for a constant pump power of approximately 100 mW is 13.7 nm, between 1562.8–1576.5 nm. A further increase in the pump power will lead to lasing at the center wavelength of the cavity. In each
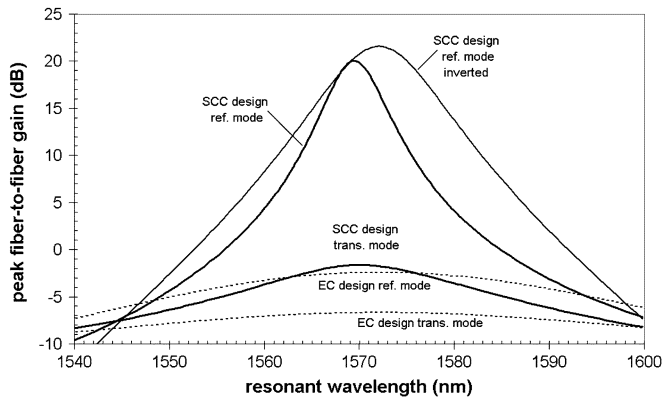
Fig. 14. Peak fiber-coupled gain for each tunable VCSOA configuration, given a peak material gain value of 1100 cm^{-1} at 1572 nm. A dashed line indicates devices utilizing the EC tunable cavity design.

Fig. 15. Peak fiber-coupled gain for the transmission-mode SCC design as well as the reflection- and transmission-mode EC-design tunable VCSOAs, given a peak material gain value of 2200 cm^{-1}. Note that the SCC-design transmission-mode device has reached lasing threshold from roughly 1558 to 1586 nm.

plot, g_{max} indicates the peak value of material gain (with a peak gain wavelength of 1572 nm). To achieve the theoretical 10-dB fiber-to-fiber tuning range mentioned above, the initial air-gap thickness must lead to a resonant wavelength ≥ 1576.5 nm, and the actuator must be capable of generating a wavelength shift ≥ 13.7 nm.

With a similar cavity design, but by using the highly reflective mirror for the MEMS tuning element $R_m = 0.999$ and using the fixed substrate DBR as the transmissive mirror $R_t = 0.974$, the 10-dB fiber-to-fiber tuning range is extended to 24.5 nm (1559.9–1584.4 nm), shown in Fig. 13(b). In both Fig. 13(a) and (b), the peak reflectance of the transmissive mirror is 0.974. Because of the increased membrane reflectance, the variation in R_{eff} with tuning is minimized, as in Fig. 9. With the inverted SCC design, the wavelength of peak fiber-to-fiber gain is found to coincide with the peak of the material gain, in contrast with the standard SCC design where the wavelength of maximum gain is determined by the peak of the effective mirror reflectance. By comparing Fig. 13(a) and (b), it is possible to see that the major limitation to the wavelength range over which sufficient signal gain may be recorded with our SCC-design reflection-mode VCSOA is attributed to the roll off in mirror reflectance with tuning.

Next, we will consider a transmission-mode device with the SCC design, utilizing the same $5\lambda_c/2$ cavity and $5\lambda_c/4$ air gap, but with equal mirror peak mirror reflectance values of $R_b = R_f = 0.974$. Applying (18), it is possible to plot the peak gain variation with tuning, included in Figs. 14 and 15 below. In this design, the peak gain response is similar to that seen in Fig. 13(a) for the SCC-design reflection-mode VCSOA, however, the increased mirror loss with transmission-mode operation leads to the requirement of higher material gain values in order to reach a similar level of signal gain. As with the previous case, the use of the transmissive mirror in the SCC tunable cavity design leads to a rapid roll off in signal gain with tuning.

Making use of our model, it is also possible to generate theoretical signal gain curves for the EC design utilizing both reflection- and transmission-mode operation. For the EC design, the change in position of the standing wave peaks with tuning must first be examined. Again, utilizing the transmission matrix solver (VERTICAL), we find that the wavelength shift for the
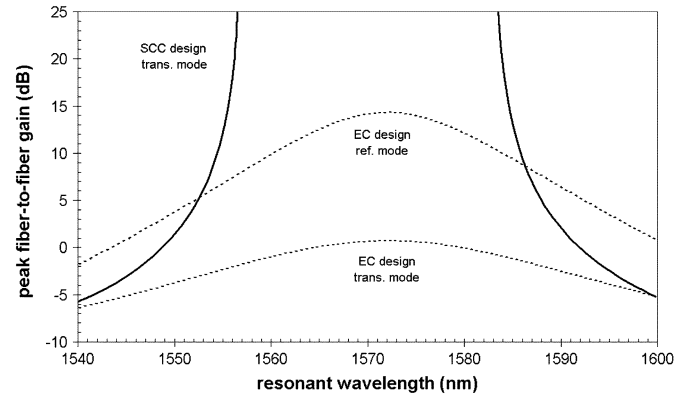
EC design with the $5\lambda_c/2$ cavity is approximately 1 nm per nm of wavelength tuning, slightly less than the value of 1.16 for a similar cavity-length SCC structure. With the EC design, the incorporation of an ideal ARC leads to $R_c \approx 0$ and $R_{eff} = R_m$, if we assume that we are using the same material structure for the membrane DBR the reflectance is reduced to a constant value of 0.91. The reduction in the reflectance of the tunable mirror structure increases the overall cavity length and leads to a reduction in the fill factor (L_a/L_c) and thus a reduction in the total confinement factor of the device. This leads to a large increase in the required g for a similar fiber-to-fiber signal gain in the EC structure.

With transmission-mode operation, the need for two transmissive mirrors leads to a further increase in the mirror loss, and in this model (again with $R_m = 0.91$) the required single-pass gain value for a signal gain of approximately 10-dB fiber-to-fiber becomes large ($>6\%$). In order to increase the achievable gain for these structures, the reflectance of the membrane should be increased to make up for removal of the air gap from the tunable mirror structure. For the EC design the signal gain response with tuning may be modeled using (17). Note that this relationship can also be used to approximate the SCC design with the highly reflective tuning mirror. As with the inverted SCC structure, the gain curves for the EC-design peak at the wavelength of maximum material gain. The gain curves for all of the modeled structures are included in Fig. 14 for a maximum material gain value of 1100 cm^{-1}. In order to generate a more useful comparison of the EC-design tunable VCSOAs, these structures have been modeled with a peak material gain value of 2200 cm^{-1} in Fig. 15. In this plot, the signal gain of the SCC-design transmission mode device has also been included.

F. Output Saturation Power and Noise Figure

Using the steady-state amplifier rate equations (7) and (8), the saturation output power as a function of the cavity resonance wavelength may be determined. In this model, the procedure outlined in [11] is employed to find the change in signal gain brought about by the increasing photon density in the resonant cavity. For any optical amplifier, the saturation output power is defined as the output signal power at which the amplifier gain is
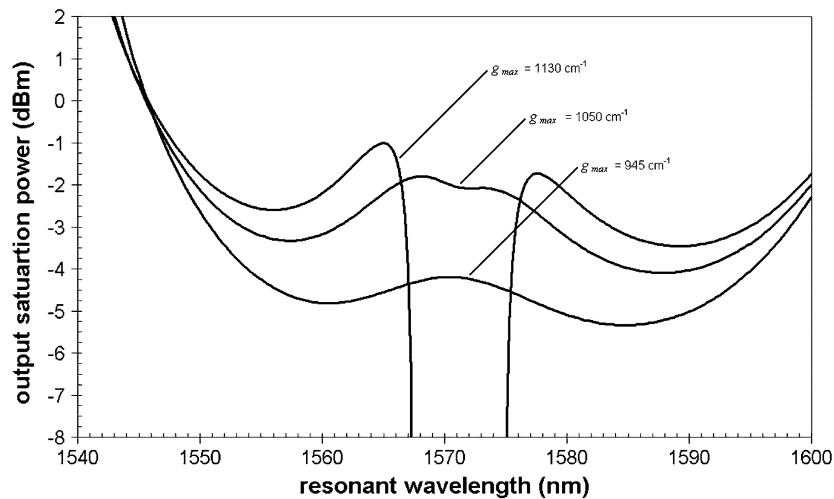
Fig. 16.   Saturation output power of the reflection mode SCC-design tunable VCSOA for various pump powers.

half of the small-signal value. The reduction in gain in this case is controlled by the rate of stimulated emission in the cavity. With increasing stimulated recombination, the photon density grows rapidly at the expense of the carrier density in the active material. From the rate equations, the stimulated emission rate is proportional to the material gain as well as the cavity photon lifetime. Over the wavelength-tuning span of the VCSOA, these parameters will vary, leading to fluctuations in the saturation characteristics of the device. The theoretical saturation output power for our SCC-design MT-VCSOA is shown in Fig. 16.

With the SCC-design tunable VCSOA, the roll off in mirror reflectance with tuning leads to a decrease in the photon lifetime, due to the increased mirror loss and thus a large increase in the saturation output power at resonant wavelengths away from the position of peak gain (for values of λ_R shorter than roughly 1550 nm and greater than about 1600 nm). Unfortunately, the amplifier gain in this regime is negligible and signal amplification is impossible. In the region of significant signal gain, from approximately 1555 to 1585 nm, and for low pump powers, the saturation output power reaches a maximum at the wavelength corresponding to the peak gain of the VCSOA (which occurs at the postion of maximum mirror reflectance for the SCC design MT-VCSOA with the transmissive tunable mirror structure). To either side of this maximum, the satuaration output power drops, and two minima are found. In this region, the mirror reflectance has increased, leading to a corresponding increase in the photon lifetime of the cavity; however, the signal gain is still low, thus limiting the output power of the VCSOA. With pump powers approaching lasing threshold, the photon density increases dramatically and the saturation output power is reduced. This is apparent for the curve corresponding to a peak gain of 1130 cm^{-1}. Here the photon density in the cavity is large enough to appreciably deplete the carrier density in the QWs, leading to a large reduction in the saturation output power of the VCSOA.

The output saturation characteristics of the other available cavity designs follow roughly the same trends as shown in Fig. 16. For the inverted SCC structure, the maximum output saturation power values are similar, as the peak mirror reflectance is the same. However, the output saturation power
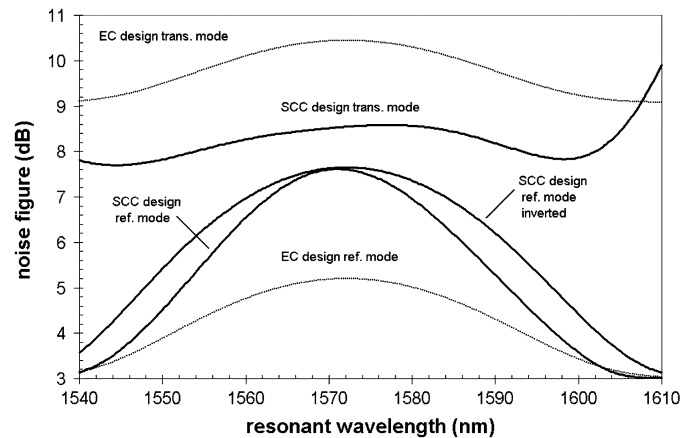

Fig. 17.   NF of each tunable VCSOA configuration given a constant peak fiber-to-fiber gain value of 10 dB over the wavelength tuning range of the amplifier.

curve is somewhat flatter around the wavelength of peak gain due to the wider range of positive signal gain values in this device. From previous work on fixed-wavelength VCSOAs, increased saturation output power is found for devices with decreased mirror reflectance, at the expense of higher required pump powers [10], [11]. The same trend holds true for the MT-VCSOA. Assuming a peak fiber-to-fiber gain of 10 dB with the SCC-design reflection-mode VCSOA, the saturation output power is roughly −2.5 dBm. For the transmission-mode SCC design the output saturation power increases to −0.5 dBm, for a similar value of peak gain, due to the increased mirror loss found in these devices. With the EC devices, the saturation output power further increases, owing to the reduction in the reflectance of the tunable mirror structure brought about by the incorporation of the ARC. These values may be compared with the recently demonstrated record high output saturation power of 0.5 dBm [41].

Much like the saturation characteristics, the NF of tunable VCSOAs will vary with tuning, due to changes in the mirror reflectance and the inherent variation in the material gain spectrum. With a VCSEL, once threshold is reached, the gain clamps at a constant value, resulting in relatively uniform properties
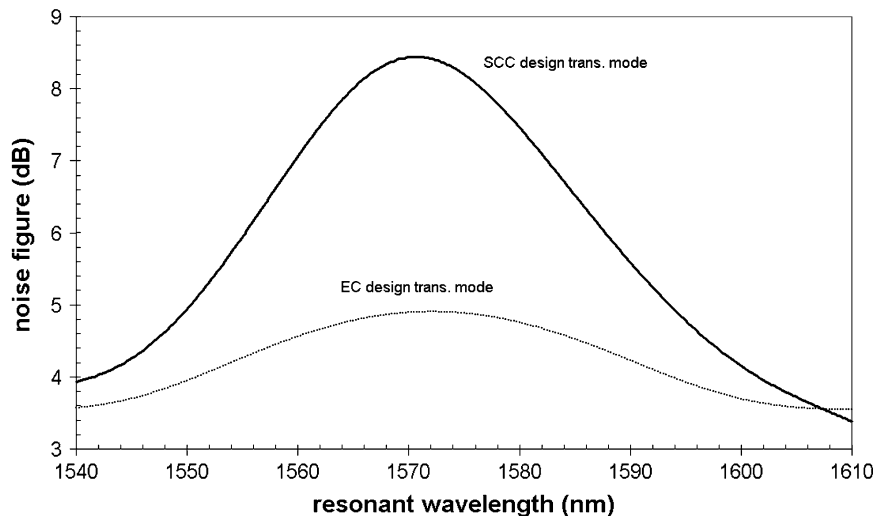
Fig. 18. NF of transmission-mode tunable VCSOAs given a constant peak fiber-to-fiber gain value of 10 dB over the wavelength tuning range. Here the input signal is injected through the opposite side of the device, so that the signal enters through a mirror with reduced reflectance values, leading to improved noise characteristics.

with tuning. With a VCSOA, on the other hand, the requirement of subthreshold operation leads to a varying value of material gain over the operating range of the device, which necessitates varying pump powers in order to maintain a constant value of signal gain. This results in a variation in the carrier density and thus a varying inversion parameter as a function of the resonant wavelength of the device (assuming a constant value of signal gain). Using the rate equations to determine the carrier density required to maintain a constant amplifier gain value with tuning, it is possible to make theoretical predictions of the noise figure of the MT-VCSOA. For this model, we have assumed that the pump power is varied in order to achieve a constant fiber-to-fiber signal gain of 10 dB. The results of this simulation are presented in Fig. 17. The effects of coupling loss have not been included in the NF calculation.

Similar to the peak gain results, the NF of the reflection-mode tunable VCSOAs exhibits a peak at the wavelength of maximum effective mirror reflectance for the SCC design with the transmissive tunable mirror structure or at the point of maximum material gain for the EC design or the SCC design with the highly reflective tunable mirror structure. With these devices, the bottom mirror reflectance value of 0.999 leads to an excess noise coefficient $\chi_r \approx 1$. Additionally, for high signal gain, $\text{NF} \approx 2n_{\text{sp}}$, and the noise figure is solely a function of the inversion parameter. For the reflection-mode devices, the required pump power is reduced near the maximum value of the active material gain and at the peak reflectance of the DBR mirrors, leading to an increase in n_{sp} and a corresponding increase in the overall noise figure. Due to the reduced variation in mirror reflectance for the inverted SCC design, the required pump power is lower for a larger range of wavelengths and thus the NF curve is somewhat broader, as compared with our standard structure. Note that the peak NF value of 7.6 dB is the same for both designs, as the peak mirror reflectance values are equal. For the EC-design reflection-mode VCSOA, the maximum NF value is reduced to 5.2 dB, as compared with the SCC-design

reflection-mode devices. This can be explained by the lower mirror reflectance and decreased optical overlap, which give rise to a higher required carrier density and a corresponding decrease in n_{sp}, for a given value of signal gain. The trend of decreased NF for lower transmissive mirror reflectance in the reflection-mode tunable VCSOAs follows the trend observed in fixed-wavelength VCSOAs [24]. Reducing the reflectance of the transmissive mirror to 0.91 in the SCC-design reflection-mode devices will result in NF values similar to that found for the EC-design reflection-mode device.

With transmission-mode tunable VCSOAs, the large mirror losses lead to the requirement of high pump powers and thus a value of n_{sp} near unity. In these devices, the excess noise coefficient is minimized for $g_s = R_b^{-1/2}$. However, the varying single-pass gain with tuning makes it difficult to operate the VCSOA under this condition. Following the results of nontunable VCSOAs, in order to optimize the NF of the transmission-mode devices, the input mirror should be of a reduced reflectance, as compared to the output mirror. This may be seen by comparing the results of Fig. 17 with the theoretical NF of the transmission-mode devices shown in Fig. 18. In this figure, the structure of the transmission-mode tunable VCSOAs is unchanged, however, the signal now enters and exits the devices in the opposite direction. This leads to a reduced NF over the tuning range of the device for the EC transmission-mode structure. In this configuration, the peak NF of the EC-design transmission-mode device is reduced to 4.9 dB. With the SCC-design transmission-mode device, the peak value of the NF is the same as that shown in Fig. 17 (8.4 dB), as the peak mirror reflectance of the tunable mirror structure is equal to the reflectance of the fixed mirror (0.974). Here the roll-off in mirror reflectance with tuning leads to the ideal condition of a reduced input mirror reflectance, reducing the NF to the extremes of the device tuning range. Note that the signal gain and required pump power are unchanged for the transmission-mode devices, regardless of the input/output signal direction.

VI. CONCLUSION

We outline here a number of possible designs for MEMS-tunable VCSOAs and compare the performance of several experimental devices to our model of the SCC-design reflection-mode VCSOA. Making use of general FP relationships, we are able to predict the wavelength tuning characteristics and the signal gain of MT-VCSOAs. Additionally, using a steady-state rate-equation approach, it is possible to describe the saturation output power and noise figure of these devices. With the VCSOA, the use of MEMS-based wavelength tuning leads to varying amplifier properties over the wavelength span of the device. The changing center wavelength of the cavity results in variations in the reflectance and penetration depth of the DBRs, changes in the confinement factor, as well as operation at different points on the material gain curve. In addition, the varying properties of the optical cavity brought about by changes in the thickness of the air gap serve to alter the device properties. For the SCC design, the changing phase of reflection from the air gap leads to largely varying mirror reflectance with tuning. With the EC design, the variation in amplifier properties is controlled by changes in the cavity length and material gain with tuning.

The major limitation to the wavelength span over which sufficient amplifier gain may be achieved in our SCC-design reflection-mode VCSOA is the roll-off in mirror reflectance that occurs as the air gap deviates from the ideal thickness. To overcome this limitation, we propose that the MEMS tuning element be used as the highly reflective DBR mirror and the fixed bottom DBR be used as the transmissive mirror in reflection-mode devices. With this design, the tuning range over which we can achieve 10 dB of fiber-to-fiber gain is increased by roughly 10 nm for a similar value of material gain. Unfortunately, a transmission-mode VCSOA requires the use of two slightly transmissive mirrors, making the varying reflectance found with the SCC design extremely difficult to avoid. With a transmission-mode tunable VCSOA, the EC design may prove to be a better choice, as the presence of the ARC in the air-cavity structure leads to a constant top mirror reflectance over the device tuning range. However, the EC design requires much larger material gain values (and corresponding optical pump powers), due to the reduction in top mirror reflectance brought about by the incorporation of the ARC in the optical cavity.

Increased saturation output powers and decreased noise figures may be achieved in devices exhibiting reduced mirror reflectance values, which is similar to fixed-wavelength VCSOAs. For the EC design, the incorporation of an ARC in the cavity results in a reduction in the effective reflectance of the tunable mirror structure and a decrease in the optical confinement factor, leading to an increase in the saturation output power, and a corresponding decrease in the signal-spontaneous beat noise. The improvement in the saturation properties and reduced noise figure come at the expense of higher required pump power values. For the SCC-design tunable VCSOA, further improvements may be found by reducing the reflectance of the transmissive mirror structure and ensuring that the highly reflective mirror reflectance remains >0.999, over the wavelength tuning range of the VCSOA.

REFERENCES

[1] E. S. Björlin, B. Riou, P. Abraham, J. Piprek, Y.-J. Chiu, K. A. Black, A. Keating, and J. E. Bowers, "Long wavelength vertical-cavity semiconductor optical amplifiers," *IEEE J. Quantum Electron.*, vol. 37, no. 2, pp. 274–281, Feb. 2001.

[2] R. Lewen, K. Streubel, A. Karlsson, and S. Rapp, "Experimental demonstration of a multifunctional long-wavelength vertical-cavity laser amplifier-detector," *IEEE Photon. Technol. Lett.*, vol. 10, no. 8, pp. 1067–1069, Aug. 1998.

[3] N. Bouché, B. Corbett, R. Kuszelewicz, and R. Ray, "Vertical-cavity amplifying photonic switch at 1.5 μm," *IEEE Photon. Technol. Lett.*, vol. 8, no. 8, pp. 1035–1037, Aug. 1996.

[4] S. Calvez, A. H. Clark, J. M. Hopkins, R. Macaluso, P. Merlin, H. D. Sun, M. D. Dawson, T. Jouhti, and M. Pessa, "1.3 μm GaInNA's optically-pumped vertical cavity semiconductor optical amplifier," *Electron. Lett.*, vol. 39, no. 1, pp. 100–102, Jan. 2003.

[5] E. S. Björlin, J. Geske, and J. E. Bowers, "Optically preamplified receiver at 10 Gb/s using a vertical cavity SOA," *Electron. Lett.*, vol. 37, pp. 1474–1475, Nov. 2001.

[6] T. Kimura, E. S. Björlin, J. Piprek, and J. E. Bowers, "High-temperature characteristics and tunability of long-wavelength vertical-cavity semiconductor optical amplifiers," *IEEE Photon. Technol. Lett.*, vol. 15, no. 11, pp. 1501–1503, Nov. 2003.

[7] M. Maute, F. Riemenschneider, G. Bohm, H. Halbritter, M. Ortsiefer, R. Shau, P. Meissner, and M.-C. Amann, "Micro-mechanically tunable long wavelength VCSEL with buried tunnel junction," *Electron. Lett.*, vol. 40, pp. 430–431, Apr. 2004.

[8] A. Syrbu, V. Iakovlev, G. Suruceanu, A. Caliman, A. Rudra, A. Mircea, A. Mereuta, S. Tadeoni, C.-A. Berseth, M. Achtenhagen, J. Boucart, and E. Kapon, "1.55-μm optically pumped wafer-fused tunable VCSEL's with 32-nm tuning range," *IEEE Photon. Technol. Lett.*, vol. 16, no. 9, pp. 1991–1993, Sep. 2004.

[9] Q. Chen, G. D. Cole, E. S. Björlin, T. Kimura, S. Wu, C. S. Wang, N. C. MacDonald, and J. E. Bowers, "First demonstration of a MEMS tunable vertical-cavity SOA," *IEEE Photon. Technol. Lett.*, vol. 16, no. 6, pp. 1438–1440, Jun. 2004.

[10] E. S. Björlin, T. Kimura, and J. E. Bowers, "Carrier-confined vertical-cavity semiconductor optical amplifiers for higher gain and efficiency," *IEEE J. Select. Topics Quantum Electron.*, vol. 9, no. 5, pp. 1374–1385, Sep.–Oct. 2003.

[11] J. Piprek, E. S. Björlin, and J. E. Bowers, "Design and analysis of vertical-cavity semiconductor optical amplifiers," *IEEE J. Quantum Electron.*, vol. 37, no. 1, pp. 127–134, Jan. 2001.

[12] C. Tombling, T. Saitoh, and T. Mukai, "Performance predictions for vertical-cavity semiconductor laser amplifiers," *IEEE J. Quantum Electron.*, vol. 30, no. 11, pp. 2491–2499, Nov. 1994.

[13] M. S. Wu, E. C. Vail, G. S. Li, W. Yuen, and C. J. Chang-Hasnain, "Tunable micromachined vertical cavity surface emitting laser," *Electron. Lett.*, vol. 31, pp. 1671–1672, Sept. 1995.

[14] M. C. Larson, A. R. Massengale, and J. S. Harris Jr., "Continuously tunable micromachined vertical-cavity surface-emitting laser with 18 nm wavelength range," *Electron. Lett.*, vol. 32, pp. 330–332, Feb. 1996.

[15] P. Tayebati, P. D. Wang, D. Vakhshoori, C. C. Lu, M. Azimi, and R. N. Sacks, "Half-symmetric cavity tunable microelectromechanical VCSEL with single spatial mode," *IEEE Photon. Technol. Lett.*, vol. 10, no. 12, pp. 1679–1681, Dec. 1998.

[16] G. L. Christensen, A. T. T. D. Tran, Z. H. Zhu, Y. H. Lo, M. Hong, J. P. Mannaerts, and R. Bhat, "Long-wavelength resonant vertical-cavity LED/photodetector with a 75-nm tuning range," *IEEE Photon. Technol. Lett.*, vol. 9, no. 6, pp. 725–727, Jun. 1997.

[17] W. S. Rabinovich, T. H. Stievater, N. A. Papanicolaou, D. S. Katzer, and P. G. Goetz, "Demonstration of a microelectromechanical tunable asymmetric Fabry–Pérot quantum well modulator," *Appl. Phys. Lett.*, vol. 83, pp. 1923–1925, Sep. 2003.

[18] J. Daleiden, N. Chitica, M. Strassner, A. Spisser, J. L. Leclercq, P. Viktorovitch, D. Rondi, E. Goutain, J. Peerlings, J. Pfeiffer, R. Reimenschneider, and K. Hjort, "Tunable InP/air gap Fabry Perot filter for wavelength division multiplex fiber optical transmission," in *Proc. 11th Int. Conf. InP and Related Materials*, May 16–20, 1999, pp. 285–287. Paper TuA3-4.

[19] D. I. Babiæ and S. W. Corzine, "Analytic expressions for the reflection delay, penetration depth, and absorptance of quarter-wave dielectric mirrors," *IEEE J. Quantum Electron*, vol. 28, no. 2, pp. 514–524, Feb. 1992.

[20] H. Ghafouri-Shiraz, *Fundamentals of Laser Diode Amplifiers*, West Sussex, U.K.: Wiley, 1996.

[21] L. A. Coldren and E. R. Hegblom, "Fundamental issues in VCSEL design," in *Vertical-Cavity Surface-Emitting Lasers*, C. W. Wilmsen, H. Temkin, and L. A. Coldren, Eds. Cambridge, U.K.: Cambridge Univ. Press, 1999, pp. 32–67.

[22] L. A. Coldren and S. W. Corzine, *Diode Lasers and Photonic Integrated Circuits*. New York: Wiley, 1995.

[23] P. Royo, R. Koda, and L. A. Coldren, "Vertical cavity semiconductor optical amplifiers: Comparison of Fabry-Perot and rate equation approaches," *IEEE J. Quantum Electron.*, vol. 38, no. 3, pp. 279–284, Mar. 2002.

[24] E. S. Björlin and J. E. Bowers, "Noise figure of vertical-cavity semiconductor optical amplifiers," *IEEE J. Quantum Electron.*, vol. 38, no. 1, pp. 61–66, Jan. 2002.

[25] M. C. Larson, "Microelectromechanical wavelength-tunable vertical-cavity light emitters and lasers," Ph.D. dissertation, Stanford Univ., Stanford, CA, 1996.

[26] P. Hariharan, *Optical Interferometry*. Sydney, Australia: Academic, 2003.

[27] F. Sugihwo, M. C. Larson, and J. S. Harris, "Micromachined widely tunable vertical cavity laser diodes," *J. Microelectromech. Syst.*, vol. 7, pp. 48–55, Mar. 1998.

[28] C.-C. Lin, W. A. Martin, and J. S. Harris, "Optomechanical model of surface micromachined tunable optoelectronic devices," *IEEE J. Sel. Topics Quantum Electron.*, vol. 8, no. 1, pp. 80–87, Jan.–Feb. 2002.

[29] S. Greek, R. Gupta, and K. Hjort, "Mechanical considerations in the design of a micromechanical tuneable InP-based WDM filter," *J. Microelectromech. Syst.*, vol. 8, pp. 328–334, Sep. 1999.

[30] W. C. Young, *Roark's Formulas for Stress and Strain*. New York: McGraw-Hill, 1989.

[31] E. K. Chan, "Characterization and modeling of electrostatically actuated polysilicon micromechanical devices," Ph.D. dissertation, Stanford Univ., Stanford, CA, 1999.

[32] L. Nicu, C. Bergaud, A. Martinez, and P. Temple-Boyer, "Static and dynamic characterization of buckled composite SiO_2-Au microbridges," in *Proc. Mat. Sci. Microelectromech. Syst. (MEMS) Devices II Mater. Res. Soc. Symp.*, vol. 605, Nov. 29–Dec. 1 1999, pp. 223–228.

[33] S. Decai, W. Fan, P. Kner, J. Boucart, T. Kageyama, Z. Dongxu, R. Pathak, R. F. Nabiev, and W. Yuen, "Long wavelength-tunable VCSEL's with optimized MEMS bridge tuning structure," *IEEE Photon. Technol. Lett.*, vol. 16, no. 3, pp. 714–716, Mar. 2004.

[34] J. A. Pelesko and D. H. Bernstein, *Modeling MEMS and NEMS*. Boca Raton, FL: Chapman and Hall/CRC, 2003.

[35] F. Sugihwo, M. Larson, and J. S. Harris Jr., "Simultaneous optimization of membrane reflectance and tuning voltage for tunable vertical cavity lasers," *Appl. Phys. Lett.*, vol. 72, pp. 10–12, Jan. 1998.

[36] A. Black, A. R. Hawkins, N. M. Margalit, D. I. Babiæ, A. L. Holmes Jr., Y.-L. Chang, P. Abraham, and E. L. Hu, "Wafer fusion: materials issues and device results," *IEEE J. Sel. Topics Quantum Electron.*, vol. 3, no. 3, pp. 943–951, Jun. 1997.

[37] S. Irmer, J. Daleiden, V. Rangelov, C. Prott, F. Romer, M. Strassner, A. Tarraf, and H. Hillmer, "Ultralow biased widely continuously tunable fabry-Perot filter," *IEEE Photon. Technol. Lett.*, vol. 15, no. 3, pp. 434–436, Mar. 2003.

[38] F. Sugihwo, "Design and fabrication of wavelength tunable optoelectronic devices," Ph.D. dissertation, Stanford Univ., Stanford, CA, 1998.

[39] P. Tayebati, P. D. Wang, D. Vakhshoori, and R. N. Sacks, "Widely tunable Fabry-Perot filter using $Ga(Al)As-AlO_x$ deformable mirrors," *IEEE Photon. Technol. Lett.*, vol. 10, no. 3, pp. 394–396, Mar. 1998.

[40] M. Strassner, N. Chitica, and A. Tarraf, "Investigations of growth conditions for InP suited for micro opto electro mechanical systems for data communication," in *Proc. 14th Int. Conf. InP and Related Materials*, May 12–16, 2002, pp. 351–354. Paper A4-5.

[41] T. Kimura, E. S. Björlin, Q. Chen, C. S. Wang, and J. E. Bowers, "High output power 1540-nm vertical-cavity semiconductor optical amplifiers," in *Proc. 16th Int. Conf. InP and Related Materials*, 31 May–4 June 2004, pp. 704–707. Paper FA2-3.

E. Staffan Björlin (M'02) received the M.S. degree in engineering physics from the Royal Institute of Technology (KTH), Stockholm, Sweden, in 2000, and the Ph.D. degree in electrical engineering from the University of California, Santa Barbara (UCSB), in 2002.

He is currently employed as a Research Engineer with Prof. J. E. Bowers at UCSB. His current research interests include vertical-cavity lasers and amplifiers, photonic integrated circuits, and integration technologies.

Qi Chen received the B.S. degree in electrical engineering and the M.S. degree from the Iowa State University, Ames, in 2000 and 2002, respectively.

He is currently an Applications Engineer with VEECO Instruments, Santa Barbara, CA.

Chung-Yeung Chan (S'04) received the B.S. degree in electrical engineering from the University of California, Santa Barbara, in 2003. He is currently working toward the M.S. degree in electrical engineering at the University of Southern California (USC), Los Angeles.

At USC, his current research involves the design and fabrication of large arrays of JFET controlled carbon nanotube field emitters.

Shaomin Wu received the B.S. degree in materials science from Fudan University in Shanghai, China, in 2001 and the M.S. degree in electrical and computer engineering from the University of California, Santa Barbara, in 2004.

His research interests include molecular beam epitaxial growth for long-wavelength vertical-cavity surface-emitting lasers. He is currently with Applied Optoelectronics Inc., Sugar Land, TX.

Garrett D. Cole was born in San Jose, CA, in 1979. He received the B.S. degree in materials engineering from the California Polytechnic State University, San Luis Obispo, in 2001. He is currently working toward the Ph.D. degree in electronic materials at the University of California, Santa Barbara.

His research focuses on the design, fabrication, and characterization of optical MEMS devices, including micromachined tunable vertical-cavity semiconductor optical amplifiers.
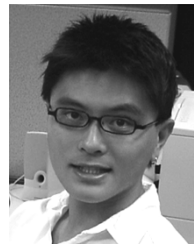
Chad S. Wang (S'99) was born in Racine, WI, in 1979. He received the B.S. degree from The University of Texas at Austin in 2001 and the M.S. degree from the University of California, Santa Barbara, in 2002, where he is currently working toward the Ph.D. degree in electrical and computer engineering.

His current research interests focus on the development of integrated laser modulators for optical interconnect applications. He is also involved in molecular beam epitaxial growth of III-V semiconductors, including vertical-cavity lasers and avalanche photodetectors.
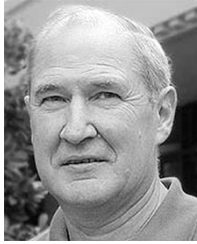
Noel C. MacDonald (S'61–M'67–SM'91–F'94) received the Ph.D. degree in electrical engineering from the University of California, Berkeley, in 1967.

He holds a joint professorial appointment with the Department of Mechanical and Environmental Engineering and the Department of Materials, University of California, Santa Barbara (UCSB), where he also holds the Fred Kavli Chair in Microelectromechanical Systems (MEMS) Technology. He has written or coauthored over 100 papers and several book chapters and holds 61 patents. He was an Acting Assistant Professor with the University of California, Berkeley, from 1967 to 1968, was a member of the Technical Staff at Rockwell International Science Center, and held management positions in Physical Electronics Industries, Inc., and Perkin-Elmer Company from 1968 to 1982. Before coming to UCSB, he held the Acheson/Laibe Professorship in Engineering at Cornell University, Ithaca, NY, and served as the Director of the Cornell Nanofabrication Facility and the Chairman of the School of Electrical Engineering at Cornell. From 1997 to 1999, he served as Director of the Microsystems Technology Office at the Defense Advanced Research Projects Agency. His current research interests include advanced materials processing as well as interdisciplinary research for micro/nano-electromechanical systems.

Prof. MacDonald is a Member of the National Academy of Engineering.

John E. Bowers (S'78–M'81–SM'85–F'93) received the M.S. and Ph.D. degrees from Stanford University, Stanford, CA.

He is the Director of the Multidisciplinary Optical Switching Technology Center (MOST) and a Professor with the Department of Electrical Engineering, University of California, Santa Barbara (UCSB). His research interests are primarily concerned with optoelectronic devices and optical networking. He is a cofounder of the Center for Entrepreneurship and Engineering Management and a cofounder of Terabit Technology and Calient Networks. He worked for AT&T Bell Laboratories and Honeywell before joining UCSB. He has published six book chapters, 350 journal papers, and 600 conference papers and holds 38 patents.

Prof. Bowers is a Fellow of the Optical Society of America and the American Physical Society. He was a recipient of the IEEE LEOS William Streifer Award and the South Coast Business and Technology Entrepreneur of the Year Award.